Suspended Sediment Dynamics in the Macrotidal Seine Estuary (France): 1. Numerical Modeling of Turbidity Maximum Dynamics

F. Grasso, R. Verney, P. Le Hir, B. Thouvenin, E. Schulz, Y. Kervella, I. Khojasteh Pour Fard, J. -P. Lemoine, F. Dumas, V. Garnier

AGU PUBLICATIONS

JGR

Journal of Geophysical Research: Oceans

RESEARCH ARTICLE

10.1002/2017JC013185

Companion to Schulz et al. [2018], https://doi.org/10.1002/2016JC012638.

Key Points:

- A realistic 3-D numerical model of mud-sand dynamics has been developed to investigate turbidity maximum dynamics of a macrotidal estuary
- The ETM location is driven by river flow and tides; the ETM mass is driven by tides and influenced more by waves than by river flow
- The neap-to-spring phasing substantially influences the ETM location and mass through a hysteresis response related to stratification, mixing, and tidal pumping mechanisms

Correspondence to:
F. Grasso,
florent.grasso@ifremer.fr

Citation:
Grasso, F., Verney, R., Le Hir, P., Thouvenin, B., Schulz, E., Kervella, Y., . . . Garnier, V. (2018). Suspended sediment dynamics in the macrotidal Seine Estuary (France): 1. Numerical modeling of turbidity maximum dynamics. *Journal of Geophysical Research: Oceans*, *123*, 558–577. https://doi.org/10.1002/2017JC013185

Received 15 JUN 2017
Accepted 12 DEC 2017
Accepted article online 28 DEC 2017
Published online 24 JAN 2018
Corrected 12 FEB 2018

This article was corrected on 12 FEB 2018. See the end of the full text for details.

Suspended Sediment Dynamics in the Macrotidal Seine Estuary (France): 1. Numerical Modeling of Turbidity Maximum Dynamics

F. Grasso[1], R. Verney[1], P. Le Hir[1], B. Thouvenin[1], E. Schulz[1,2], Y. Kervella[3], I. Khojasteh Pour Fard[1,4], J.-P. Lemoine[5], F. Dumas[1,6], and V. Garnier[7]

[1]IFREMER – DYNECO/DHYSED, Centre de Bretagne, Plouzané, France, [2]Department of Physical Oceanography and Instrumentation, Leibniz Institute for Baltic Sea Research Warnemünde (IOW), Warnemünde, Germany, [3]OPEN OCEAN, Recherche et Développement, Brest, France, [4]Now at University of Isfahan, Isfahan, Iran, [5]Groupement d'Intérêt Public Seine-Aval, Pôle Régional des Savoirs, Rouen, France, [6]Now at Service Hydrographique et Océanographique de la Marine, Brest, France, [7]IFREMER, Univ. Brest, CNRS, IRD, Laboratoire d'Océanographie Physique et Spatiale, IUEM, Plouzané, France

Abstract Tidal pumping, baroclinic circulation, and vertical mixing are known to be the main mechanisms responsible for the estuarine turbidity maximum (ETM) formation. However, the influence of hydrometeorological conditions on ETM dynamics is still not properly grasped and requires further investigation to be quantified. Based on a realistic three-dimensional numerical model of the macrotidal Seine Estuary (France) that accounts for mud and sand transport processes, the objective of this study is to quantify the influence of the main forcing (river flow, tides, and waves) on the ETM location and mass changes. As expected, the ETM location is strongly modulated by semidiurnal tidal cycles and fortnightly time scales with a high sensitivity to river flow variations. The ETM mass is clearly driven by the tidal range, characteristic of the tidal pumping mechanism. However, it is not significantly affected by the river flow. Energetic wave conditions substantially influence the ETM mass by contributing up to 44% of the maximum mass observed during spring tides and by increasing the mass by a factor of 3 during mean tides compared to calm wave conditions. This means that neglecting wave forcing can result in significantly underestimating the ETM mass in estuarine environments. In addition, neap-to-spring phasing has a strong influence on ETM location and mass through a hysteresis response associated with the delay for tidal pumping and stratification to fully develop. Finally, simulations show that the uppermost limit of the Seine ETM location did not change notably during the last 35 years; however, the seaward limit migrated few kilometers upstream.

1. Introduction

The estuarine turbidity maximum (ETM) is a key pattern in worldwide macrotidal estuarine sediment dynamics (e.g., Delaware Estuary [USA] [McSweeney et al., 2016], Gironde Estuary (France) [Jalón-Rojas et al., 2015], and Yalu Estuary (China) [Yu et al., 2014]). This zone of high suspended sediment concentration (SSC) buffers sediment exchanges between continental and coastal waters, controls channel siltation, and drives biogeochemical processes (Billen et al., 2007; Passy et al., 2016).

Many studies investigated ETM dynamics from in situ measurements (Jalón-Rojas et al., 2015, 2016; McSweeney et al., 2016; Sottolichio et al., 2011) and/or numerical modeling (Bi & Toorman, 2015; Le Hir et al., 2001; Sottolichio et al., 2000; Toublanc et al., 2016; Winterwerp, 2011; Yu et al., 2014). They enabled the characterization of the major mechanisms for ETM formation as: (i) the "tidal pumping" induced by the tidal asymmetry between stronger flood-tide velocity and weaker ebb-tide velocity and (ii) the upward bottom residual transport induced by longitudinal salinity gradients between the fresh river flow and the saline seawater (Allen et al., 1980; Brenon & Le Hir, 1999; Dronkers, 1986; Dyer, 1973; Scully & Friedrichs, 2007; Uncles & Jordan, 1979; Yu et al., 2014). Moreover, the tidal variations of turbulent mixing, with enhanced vertical mixing during the flood and suppressed mixing during the ebb phase (Simpson et al., 1990), modify the vertical distribution of particles, which are likely to settle more easily on ebb (Burchard & Baumert, 1998; Burchard & Hetland, 2010). Turbulent mixing also decays from the upper estuary down to the stratified saline intrusion zone, so that sediment settling (and trapping) is enhanced in the latter area (Geyer, 1993).

Recently, Toublanc et al. (2016) concluded that, in the highly turbid Charente Estuary (with SSCs often exceeding 5 g/L), the tidal asymmetry was the main mechanism leading to the ETM formation, whereas the density gradients contributed to maintaining the ETM stability. Vertical stratification trapped sediment at the bottom and the longitudinal density gradients ensured a sharper concentration gradient at the downstream limit of the ETM, preventing a massive export of sediments.

The ETM location is known to be strongly modulated by the river flow and the tidal amplitude (Allen et al., 1980; Avoine et al., 1981; Sommerfield & Wong, 2011; Uncles & Stephens, 1989; Van Maren & Hoekstra, 2004). It varies over the tidal cycle, with increasing excursion during spring tides. However, the tide-averaged location is mainly related to the river flow, translated downstream during higher river flow and potentially flushed out for river flood events. The ETM mass results from a combination of the mechanisms described previously. Tidal pumping increases during spring tide, as tidal asymmetry and currents increase. Contrarily, the sediment trapping can be more pronounced during neap tide when the hydrodynamics are less energetic and the stratification is stronger. Waves may also significantly affect the ETM dynamics (Le Hir et al., 2001), resuspending flushed-out ETM sediment and hence accelerating ETM reformation. However, this forcing is rarely investigated from in situ measurements or realistically taken into account in numerical modeling, resulting in a lack of understanding on the wave contribution to ETM dynamics.

Based on a realistic three-dimensional (3D) process-based numerical model, this study investigates the suspended sediment (mud/sand) dynamics of the macrotidal Seine Estuary (France). The objective is to quantify the ETM location and mass sensitivity to different hydrodynamic (tide) and hydrological (river flow) forcing with an interest on wave effects. With the development and use of upgraded codes for hydrodynamics, wave simulation, and sediment dynamics, the numerical modeling differs significantly from previous work on the Seine Estuary (Le Hir et al., 2001). Numerical modeling setup and in situ measurement data set are described in section 2. Section 3 presents the validation of the numerical model based on hydrodynamics and suspended sediment dynamics. The discussion in section 4 addresses the quantification of ETM location and mass changes under different forcing and conclusions are presented in section 5.

This study is associated with a companion paper Schulz et al. (2018). While the present Part 1 focuses on the ETM dynamics from semidiurnal tidal cycle to hydrological time scales, Part 2 focuses on the quantification of sediment fluxes and budgets along the lower estuary, from wave events to annual time scales, for typical hydro-meteorological years (i.e., average, dry, wet, and stormy).

2. Material and Methods

2.1. Study Area

The macrotidal Seine Estuary, located in the Northwestern part of France, is characterized by a semidiurnal tidal range reaching 8 m at Le Havre (LH in Figure 1a). It is one of the largest estuaries on the Northwestern European continental shelf, with a catchment area of more than 79,000 km^2. The estuary stretches from the Bay of Seine open to the English Channel to the weir of Poses upstream, limit of the tidal influence. The Seine river flow (Q) ranges from 100 to 2,300 m^3/s in low and high river flow periods, respectively, with a mean annual flow around 450 m^3/s computed over the last 20 years. Accordingly, the Seine sediment supply ranges from 1 to 900 kg/s, with a mean sediment supply of 23 kg/s corresponding to 725×10^6 kg/yr (Schulz et al., 2018, Figure 1).

During the last two centuries, the Seine Estuary has been vastly altered by human activity (Avoine et al., 1981). As a result, the lower Seine River was changed from a dominantly natural system to an anthropogenically controlled system. The funnel-shaped estuary is exposed to western winds, so that the intertidal regions at the mouth are subject to erosion under the combined effect of waves and currents (Deloffre et al., 2007; Verney et al., 2007). The dominant wind direction is from southwest with average wind speeds of about 4 m/s and peaks of more than 15 m/s. Waves enter the bay from northwest with typical significant wave heights of 0.5 m and peaks of more than 3.5 m in front of the estuary mouth. Schulz et al. (2018) provide a detailed description of wind and river flow forcing on the Seine Estuary over the last 20 years. The lower estuary is characterized by the presence of an ETM that has a pronounced control on the sedimentation patterns of subtidal areas and intertidal mudflats from the estuary mouth up to the upstream freshwater limit, which is few kilometers downstream of Caudebec-en-Caux (C in Figure 1a) (Avoine et al., 1981; Deloffre et al., 2005; Le Hir et al., 2001).

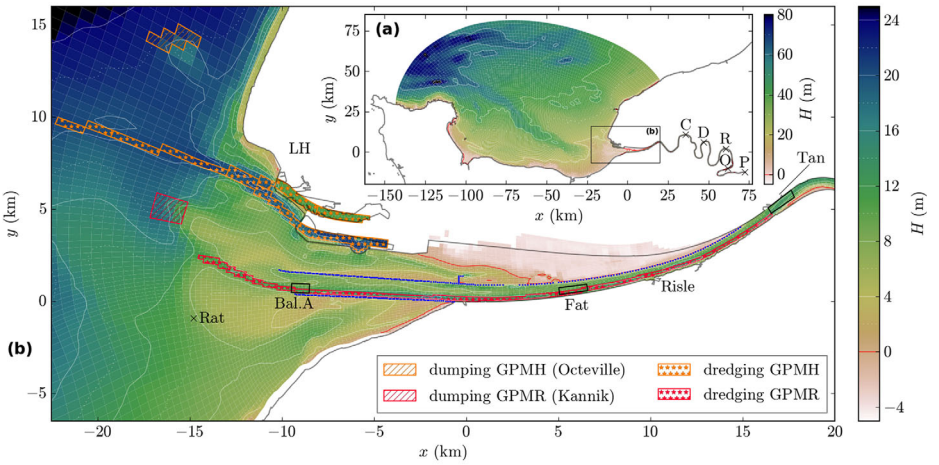

Figure 1. Bathymetry (mean sea level chart datum) of the Seine Estuary numerical model: (a) extending from the Bay of Seine to the weir of Poses "P" and (b) a zoom on the lower estuary. Dredging (stars) and dumping (hatching) areas for the Grands Ports Maritimes du Have "GPMH" (orange) and Rouen "GPMR" (red). The black boxes at Balise A "Bal.A," Fatouville "Fat," and Tancarville "Tan" represent comparison areas for measured and simulated SSC. Specific locations: Le Havre "LH," Ratelets "Rat," Caudebec-en-Caux "C," Duclair "D," Rouen "R," and Oissel "O."

2.2. Numerical Model Setup

2.2.1. Hydrodynamic Model

A 3-D numerical model has been developed to study the hydro and sediment dynamics of the Seine Estuary from the offshore limit of the Bay of Seine to the weir of Poses (Figure 1a), with a particular interest on the lower estuary from the mouth to Tancarville, corresponding to the main area of the ETM excursion. A nonorthogonal curvilinear mesh was chosen to better respect the estuarine shape, to optimize the computation costs by lengthening the meshes in the direction of dominant tidal flows, and to improve sediment flux estimates (Kervella et al., 2012; Khojasteh Pour Fard, 2015). Cells range from around 30 × 100 m^2 at the estuary mouth to 2 × 2 km^2 offshore and the bathymetry corresponds to the year 2010 (mean sea level chart datum).

The hydrodynamic model is based on the hydrostatic model MARS3D coupling barotropic and baroclinic modes (Lazure & Dumas, 2008). The water column is discretized with 10 equidistant sigma layers and adaptive time steps range from 2 to 18 s. Turbulence closure is based on a mixing length model that accounts for turbulence damping by density gradients (Cugier & Le Hir, 2002). The circulation model is forced by the main tidal components at the sea boundary extracted from the CST France database (Service Hydrographique et Océanographique de la Marine, SHOM) and wind stresses and pressure gradients provided by the meteorological ARPEGE model (Meteo-France). The realistic Seine and Risle river flows are prescribed at Poses and at the Risle mouth (Figure 1), respectively. Waves are simulated using the WAVE WATCH III® (WW3) model (Roland & Ardhuin, 2014) on a series of embedded computational grids, from a large-scale model of the Atlantic Ocean down to a local model at the same resolution as the circulation model. Wave simulations are forced by the free surface elevation and the current velocities provided by MARS3D. The wave-induced bed shear stress (τ_w) is computed from the bottom orbital velocity components (u_b and v_b) as $\tau_w = \frac{1}{2}\rho f_w U_w^2$ (Jonsson, 1966), with $\rho = 1{,}025$ kg/m^3 the water density, f_w the wave friction parameter (see Table 1) and the orbital wave velocity $U_w = \sqrt{u_b^2 + v_b^2}$. The current-induced bed shear stress (τ_c) is computed as $\tau_c = \rho u_*^2$ where u^* is estimated from the logarithmic

Table 1
Main Calibration Parameters that Were Used to Optimize the Validation of the Realistic 3-D Numerical Model Used in This Study

Parameter	Value
f_w	0.015
$z_{0\ sed}$ (mm)	0.5
z_0 (mm)	0.1–25
n_{sand}	1.6
n_{mud}	1
$E_{0,mud}$ (kg/m^2/s)	3.10^{-4}
α_1	10^{-5}
α_2	2
$w_{s,min}$ (mm/s)	0.1
$w_{s,max}$ (mm/s)	1.5
A	0.3
B	0.18
c_1	3.10^{-3}
c_2	0.79

boundary layer theory $u(z)=\frac{u^*}{\kappa}\ln\left(\frac{z}{z_{0\,sed}}\right)$ with $u(z)$ the bottom water cell velocity at elevation z and $z_{0\,sed}$ the skin bottom roughness length characteristic of the estuary mouth sediment (see Table 1). The total bed shear stress (τ) is computed as a combination of the current- and wave-induced bed shear stresses (Soulsby, 1997; equations 69 and 70), which reads:

$$\tau=\left[\left(\tau_{cw}+\tau_w|\cos\Phi|\right)^2+\left(\tau_w\sin\Phi\right)^2\right]^{1/2} \tag{1}$$

$$\tau_{cw}=\tau_c\left[1+1.2\left(\frac{\tau_w}{\tau_c+\tau_w}\right)^{3.2}\right] \tag{2}$$

with Φ the angle between the current and the orbital wave velocities and τ_{cw} the current-induced bed shear stress influenced by waves.

2.2.2. Sediment Model

The hydrodynamic model is coupled with a process-based sediment model for sand and mud mixtures (Le Hir et al., 2011). The sediment bed is discretized with a maximum of 100 layers of variable thickness ranging from 1 μm to 5 mm. This multilayer model accounts for the spatial and temporal variations of sand and mud content in the sediment, as well as for consolidation processes. In the water column, the model resolves advection/diffusion equations for different classes of particles. In this study, five classes of sediment representative of the Seine Estuary sediment modes were initially distributed over a 1 m thick bed according to the measured sediment distribution (Lesourd et al., 2015): one gravel (diameter $d=5$ mm), three sands ($d=800$ μm, $d=210$ μm, $d=100$ μm), and one mud ($d=20$ μm). The mud advection is calculated by means of a complete 3-D scheme with a variable settling velocity accounting for flocculation processes (Van Leussen, 1994):

$$w_{s,mud}=\max\left[w_{s,\min},\ \min\left(w_{s,\max},\ c_1C_{mud}^{c_2}\frac{1+aG}{1+bG^2}\right)\right] \tag{3}$$

with C_{mud} the mud concentration, G the turbulent shear rate, and a, b, c_1, c_2 calibration parameters (see Table 1). The mud settling velocity was minimized ($w_{s,min}$) and maximized ($w_{s,max}$) according to in situ measurements carried out in the Seine Estuary in the framework of the FLUMES project (Seine-Aval 4 research program). Contrastingly, the gravel and sand classes have a constant settling velocity depending on their diameter (Soulsby, 1997, equation 102). These sand classes are transported as depth-averaged variables with the bottom flow, assuming that the vertical profile of sand concentration follows an equilibrium Rouse profile, in order to avoid excessive computational costs for the vertical advection of heavy particles.

The erosion flux is based on the formulation from Partheniades (1965):

$$\begin{cases}\tau>\tau_e\Rightarrow E=E_0\left(\frac{\tau}{\tau_e}-1\right)^n\\ \tau<\tau_e\Rightarrow E=0\end{cases} \tag{4}$$

with E the erosion rate, E_0 an erosion parameter τ_e the critical erosion stress, and n a calibration parameter. To represent mixed-sediment processes, the erosion flux computation depends on the mass fraction of mud (f_m) (Le Hir et al., 2008; Panagiotopoulos et al., 1997). For f_m lower than 0.3, the sediment is defined as noncohesive: $n=n_{sand}$ (Table 1), τ_e is computed as the critical erosion stress of sand ($\tau_{e,sand}$) following the Shields criteria (Soulsby, 1997, equation 76), and E_0 is computed as the sand erosion parameter E_{0sand}, derived from erodibility measurements (Le Hir et al., 2008), which reads:

$$E_{0,sand}=\tau_{e,sand}^{n_{sand}}\min\left(0.27\ ,\ 10^3\langle d_{50,sand}\rangle-0.01\right) \tag{5}$$

where $\langle d_{50,sand}\rangle$ is the median diameter of the sand classes in the upper eroded layer. For f_m larger than 0.7, the sediment is defined as cohesive: $n=n_{mud}$, $E_0=E_{0,mud}$ the erosion parameter of mud, and $\tau_e=\tau_{e,mud}$ the critical erosion stress of mud expressed as:

$$\tau_{e,mud}=\alpha_1C_{relmud}^{\alpha_2} \tag{6}$$

with α_1 and α_2 empirical parameters (Table 1), and the relative mud concentration

$$C_{relmud} = \frac{C_{mud}}{1-\phi_{sand}} \quad (7)$$

related to the mud mass concentration (C_{mud}) and the sand (and gravel) volumetric concentration (ϕ_{sand}). The relative mud concentration can be seen as the mud concentration in the space not occupied by sand and gravel (Sanford, 2008; Waeles et al., 2008). The critical erosion rate of mud, related to C_{relmud}, depends on the state of consolidation of the sediment. Therefore, the sediment model is coupled with a consolidation module resolving the Gibson equation for mixed sediments, taking into account segregation processes, permeability and effective stress regimes of the sedimentation/consolidation phases (Grasso et al., 2015). Mud/sand mixtures from the Seine Estuary were used to validate this consolidation module. Finally, for $0.3 < f_m < 0.7$, the erosion law parameters are linearly interpolated between the cohesive and noncohesive behaviors. Le Hir et al. (2011) provide a detailed description of the sediment model; the main numerical model set-up and calibration parameters used in this study are defined in Table 1.

The maintenance of Le Havre (Grand Port Maritime du Havre [GPMH]) and Rouen (Grand Port Maritime de Rouen [GPMR]) harbors, and their channel access (Figure 1b), requires large sediment dredging and dumping activities in the lower estuary ($\sim 5.4 \times 10^9$ kg/yr) (Marmin et al., 2014). Such sediment transfers are important compared to the Seine sediment supply (0.7×10^9 kg/yr) and have to be taken into account to properly simulate the Seine Estuary sediment dynamics. The dredging/dumping activities are carried out every day to maintain a water depth assuring ship navigation to GPMH and GPMR. In this study, the sediment model simulates these actions by removing the upper sediment layers (mud and sand) in the dredged areas (Figure 1) every 10 min, as consolidation time steps, if the sediment deposit exceeds a prescribed base elevation corresponding to the minimal required water depth provided by the GPMH and GPMR. The dredged sediment mass is then released in the lowest cells of the water columns associated with the dumping areas, namely Octeville for the GPMH and Kannik for the GPMR (Figure 1b). Such a modeling approach enables anthropogenic sediment transfer to be taken into account.

The Seine sediment supply is imposed at Poses at the same location as the river flow and is composed of the mud fraction. This mud flux, presented in Schulz et al. (2018), varies with the Seine river flow following a relation based on Avoine et al. (1981) formula. Avoine et al. (1981) made a distinction between high river flow ($SPM_H = 10^{-6} * Q^{1.66}$ g/L) and low river flow ($SPM_L = 3.4 \times 10^{-5} * Q + 7.797$ g/L), based on a river flow threshold (Q_{th}). This relation has been improved by using SPM_H for river flow larger than $Q_{th} = 900$ m^3/s and increasing (before the flood peaks) as well as SPM_L for river flow smaller than Q_{th} or decreasing (after the flood peaks). Such a method takes into account the sediment suspension hysteresis between pre- and post-flood events. The formula has been validated on three-year daily SSC measurements (2001–2003) with the Seine river flow ranging from 100 to 2,200 m^3/s and the SSC ranging from 0.01 to 0.37 g/L. It presents good skills (square correlation coefficient $r^2 = 0.69$ and root-mean-square error $e_{rms} = 0.022$ g/L), noticeably improving the previous formulation ($r^2 = 0.41$; $e_{rms} = 0.062$ g/L). In the present Part 1, as in Schulz et al. (2018), the new formula is applied to the measured Seine river flow to estimate the mud flux at the upstream boundary.

2.3. In Situ Measurements

In situ measurements were used as reference data for the calibration and validation of the numerical model. Hydrodynamics and hydrology surveys were carried out from August 2010 to August 2011 in the framework of the MODEL project (Seine-Aval 4 research program), associated with a mean annual flow of 426 m^3/s representative of the last 20 years (450 m^3/s). Water surface elevations (Figure 2), measured by the GPMR tidal gauges, were collected at six locations in order to represent the upstream increase of the tidal asymmetry (from the sea upward: Balise A, Fatouville, Tancarville, Figure 1b; Caudebec-en-Caux, Duclair, Oissel, Figure 1a). The salinity gradient (Figure 3) was measured from bottom (3 m above the bed) and surface (1 m below the surface) conductivity sensors at Fatouville pier, which is located at the Seine River southern shore approximately at the center of the ETM longitudinal excursion (Figure 1b). Wave parameters, as the significant height H_s and the orbital velocity U_w (Figure 4), were estimated from a wave pressure sensor located at the bottom of the Ratelets station (indicated in Figure 1b).

The SYNAPSES monitoring network, managed by the Groupement d'Intérêt Public Seine-Aval (GIPSA), provided bottom (1 m above the bed) turbidity measurements from August 2014 to August 2015, associated with a mean annual flow of 516 m^3/s, also representative for the last 20 years. This study focused on the

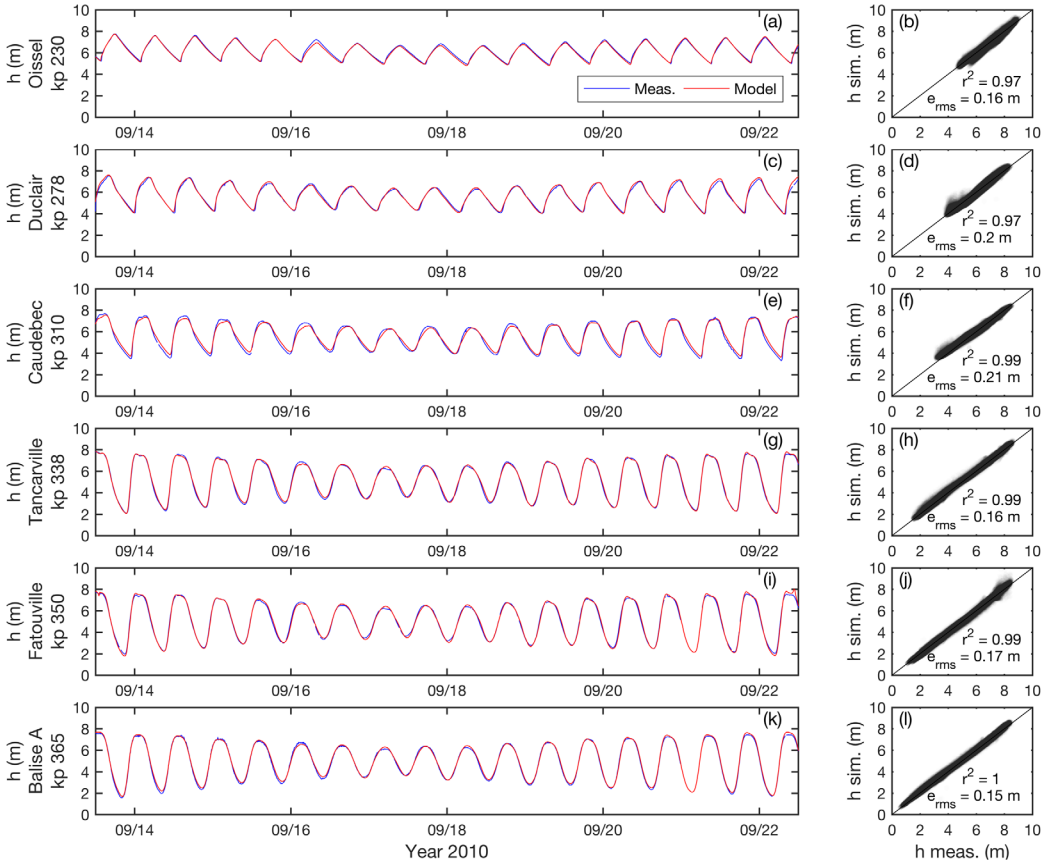

Figure 2. Water surface elevations h at (a, b) Oissel, (c, d) Duclair, (e, f) Caudebec-en-Caux, (g, h) Tancarville, (i, j) Fatouville, and (k, l) Balise A (see locations in Figure 1). (left) Measurements (blue) and simulations (red) from 14 to 22 September 2010. (right) Simulations versus measurements from August 2010 to August 2011, with the correlation coefficient squared r^2 and the root-mean-square error e_{rms}. kp are the kilometric points along the Seine River, defined as 0 in Paris.

three stations located in the ETM longitudinal excursion: the Balise A buoy, the southern shore Fatouville pier, and the northern shore Tancarville pier (Figure 1b). SSCs (g/L) were derived from turbidity measurements (nephelometric turbidity unit) according to a calibration coefficient (c_{cal}). c_{cal} was estimated from 565 in situ water samples collected at Fatouville and Tancarville between January 2015 and June 2016. In this study, the mean coefficient $c_{cal} = 0.00121$ associated with the error margin of 50% is used.

Note that the Fatouville and Tancarville monitoring stations are located at pier bases close (15 m) to the rock-filled shore. The large roughness induced by the rocky shore (and the pier pillars) is likely to increase resuspension and to enhance local SSC. Such a very local behavior is expected to be not fully representative of the SSC in the channel, especially around low tide, and has to be discussed accordingly.

3. Validation of the Numerical Model

The numerical model results presented in this study were obtained from simulations that were ran after a 1 year spin-up. This means that the simulation results after 1 year (i.e., hydrodynamics, salinity, SSC, sediment bed) were used as initial conditions for running the reference year. With the reference year similar to the spin-up year, this guarantees a sufficient model robustness and conservativity for simulating the suspended sediment dynamics and especially the ETM at hydrological time scales. Simulation outputs were saved every 15 min to enable an accurate description of the processes driven by short and energetic forcing, as tidal flood, for instance.

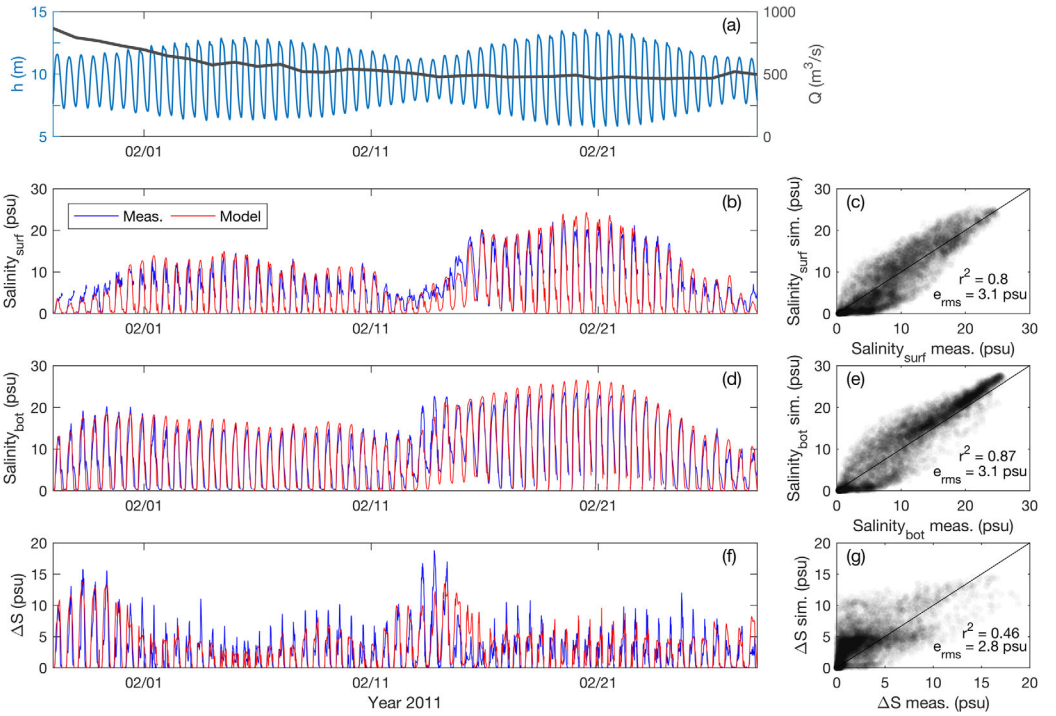

Figure 3. (a) Water level h simulated at Fatouville (blue) and Seine river flow Q measured at Poses (dark gray). (b, c) Surface salinity, (d, e) bottom salinity, and (f, g) vertical salinity gradient ΔS at Fatouville. (b, d, f) Measured (blue) and simulated (red) salinity, from 28 January 2011 to 28 February 2011. (c, e, g) Simulations versus measurements from September 2010 to May 2011, with the correlation coefficient squared r^2 and the root-mean-square error e_{rms}.

3.1. Hydrodynamics

In a macrotidal environment, such as the Seine Estuary with a tidal range approaching 8 m at Le Havre, tidal currents represent one of the main forcing on sediment dynamics. The tidal asymmetry between ebb and flood current peaks increases as the tide propagates up-estuary and is known to contribute significantly to the ETM formation and dynamics (Brenon & Le Hir, 1999; Dyer, 1973; Toublanc et al., 2016; Yu et al., 2014). To properly simulate this "tidal pumping" mechanism, it is crucial to correctly simulate the tide propagation along the estuary that can be characterized by the water surface elevation (Figure 2). The longitudinal locations are expressed in kilometric points (kp) along the Seine River, defined as 0 in Paris and increasing seaward. It is clearly readable from the tidal gauge measurements (blue) that the tidal asymmetry increases and the tidal range decreases from the estuary mouth (Balise A, kp 365, Figure 2k) toward the estuary's upstream limit close to Poses (Oissel, kp 230, Figure 2a). The simulated water levels from the Bay of Seine to the upper estuary at Poses were calibrated by adjusting the form bottom roughness length ($z_0 = 0.1$–25 mm, Table 1) in different portions of the model domain. The spatially varying bed roughness is based on the sediment grain size distribution at the mouth and offshore (Lesourd et al., 2015); in the channel, it has been adjusted by trial and error. As a result, the water level at the different locations along the estuary was very well simulated (red) with high skills over the entire measurement period (from September 2010 to May 2011, $r^2 = 0.97$–1.00, and $e_{rms} = 0.15$–0.20 m), particularly in the lower estuary where the ETM occurs (Figures 2g–2l). Therefore, a significant confidence in the model ability to properly simulate the tidal pumping is provided.

3.2. Salinity

The salinity front between the fresh Seine River and the salty seawaters has a major influence on ETM formation as well. The longitudinal salinity gradient induces an upward bottom residual transport and the vertical salinity gradient, characteristic of stratification, modifies the vertical distribution of particles (Brenon & Le Hir, 1999; Burchard & Baumert, 1998; Dyer, 1973; Toublanc et al., 2016; Yu et al., 2014). At Fatouville station, which is located within the ETM tidal excursion during low to high river flow, the salinity dynamics in the whole water column were observed to be strongly modulated by the semidiurnal tidal cycles and

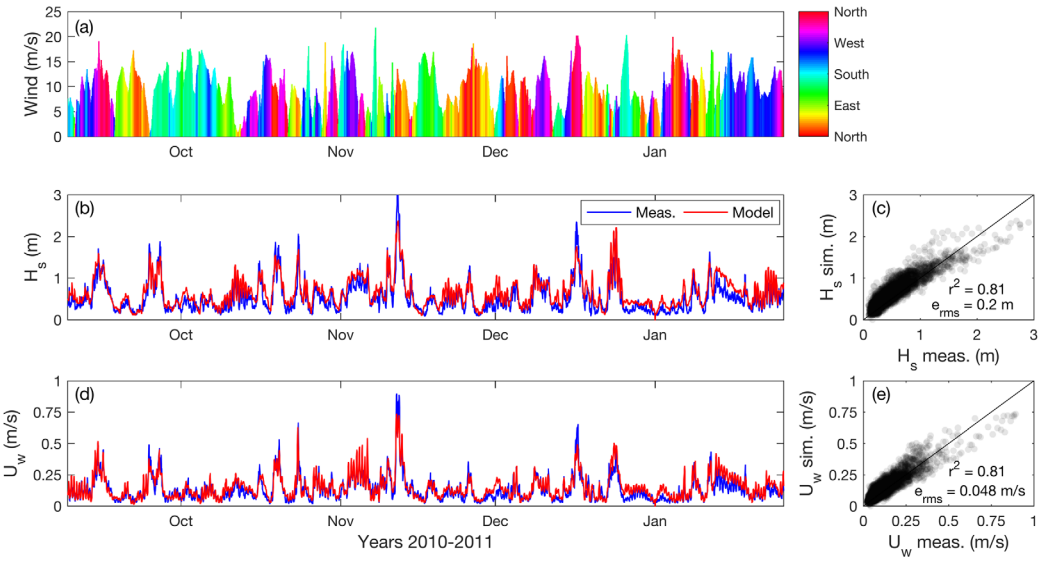

Figure 4. Wind and wave conditions at the Ratelets station from September 2010 to January 2011. (a) Wind speed and origin direction (color bar), (b, c) significant wave height H_s, and (d, e) orbital wave velocity U_w, with (b, d) measurements in blue and simulations in red and (c, e) simulations versus measurements with the correlation coefficient squared r^2 and the root-mean-square error e_{rms}.

fortnightly time scales (blue, Figures 3b and 3d). It ranged from fresh (0 psu) to salty (up to 30 psu) water over a single semidiurnal tidal cycle. The water column stratification, characterized by the difference between the bottom and surface salinity ($\Delta S = S_{bot} - S_{surf}$), increased for low-energetic periods, such as neap tide (Figure 3f). The measured salinity (blue) is well reproduced by the simulation (red) with good skills (Figures 3b–3e), both near surface and bottom ($r^2 = 0.84$–0.88, $e_{rms} = 3.0$–3.4 psu). The model tends to overestimate the bottom salinity during spring tide and to underestimate the surface salinity from neap-to-spring tide, which results in simulating ΔS with lower skills ($r^2 = 0.46$, $e_{rms} = 2.8$ psu). Nevertheless, the model was able to reasonably well simulate the salinity gradient magnitude and dynamics from tidal to hydrological time scales.

3.3. Wave Dynamics

Wind waves generated by local winds in the Bay of Seine and swells coming from the North-Atlantic Ocean contribute to the total bed shear stress (equation (1)) and may have a significant impact on sediment resuspension (Le Hir et al., 2001; Verney et al., 2007). Wave-induced bed shear stress can be dominant over the current-induced bed shear stress on the sand banks and intertidal mudflats at the estuary mouth and may affect the ETM dynamics during storm events. Wave measurements at the Ratelets station (Figure 4b), located seaward of the Southern bank at the mouth, recorded large waves (significant height H_s reaching 3 m) occurring in shallow water (3–11 m deep). Note that the largest waves were observed for winds from SW and NW, as expected from the orientation of bay and estuary (Figure 4a). The WW3 model, taking into account wind waves and offshore swells, achieved good skills to simulate the significant wave height ($r^2 = 0.81$, $e_{rms} = 0.20$ m), with a small underestimation of the largest wave events. Prediction skills for simulating the orbital wave velocity were also very good ($r^2 = 0.81$, $e_{rms} = 0.05$ m/s). Consequently, the wave-induced bed shear stress computation derived from U_w simulated by WW3 was integrated in the total bed shear stress computation (equations in section 2.2.1) with confidence.

3.4. Suspended Sediment Dynamics

The main interest of this study concerns the suspended sediment dynamics of the Seine Estuary, focusing on the lower part from Balise A to Tancarville where the ETM is located. To filter out small-scale spatial variability of the model results, outputs were averaged over 5 × 5 cell areas (Figure 5) centered on Balise A, Fatouville, and Tancarville measurement locations, as presented in Figure 1b. In addition, the minimum and maximum values of these boxes were analyzed to indicate the variability over small longitudinal (∼1 to 2 km) and transversal (∼400 to 500 m) distances (Figure 6).

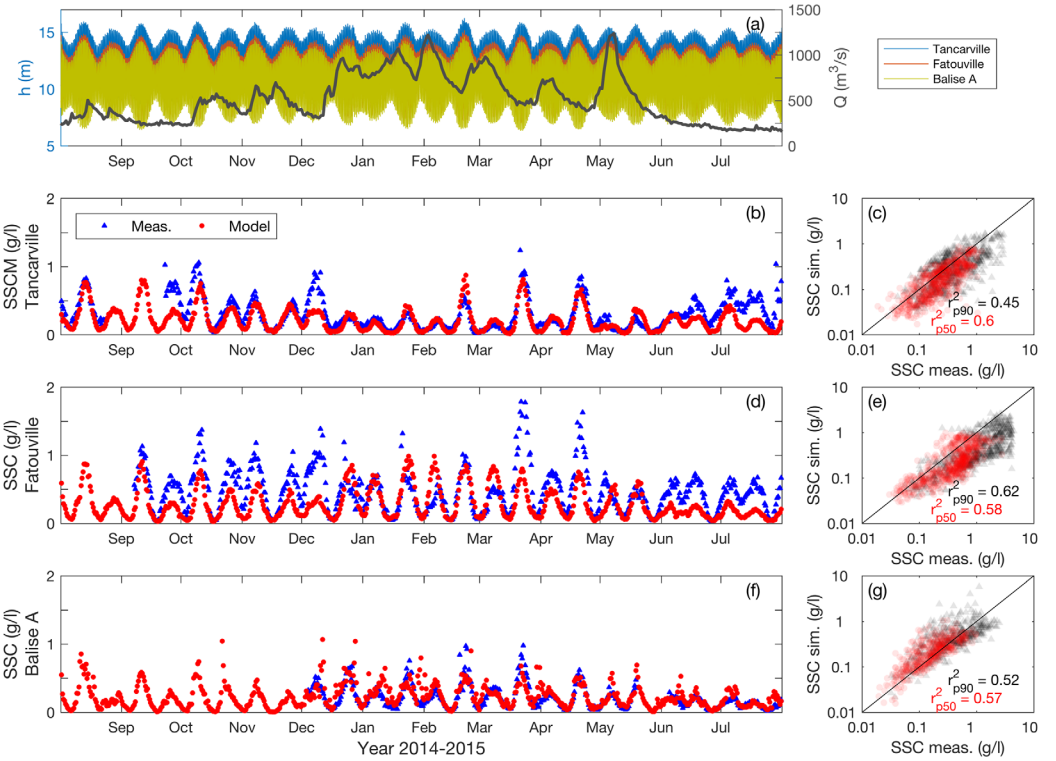

Figure 5. Tide-averaged near-bottom SSC dynamics from August 2014 to August 2015. (a) Seine river flow *Q* (gray) and water depth *h* at Balise A (green), Fatouville (red), and Tancarville (blue). (b, d, f) Measured (blue triangles) and simulated (red circles) median SSC (i.e., 50th percentile), and (c, e, g) simulated versus measured 50th percentile (red) and 90th percentile (black) SSC at (b, c) Tancarville, (d, e) Fatouville, and (f, g) Balise A.

3.4.1. Tide-Averaged Suspended Sediment Dynamics

Figure 5 illustrates the tide-averaged (i.e., 15 min data averaged from peak low tide to consequent peak low tide) near-bottom (1 m above bed level) median (i.e., 50th percentile) SSC from August 2014 to August 2015 at Tancarville (Figure 5b), Fatouville (Figure 5d), and Balise A (Figure 5f). The measured SSC dynamics (blue) were strongly modulated by fortnightly time scales, with increasing magnitude during spring tides. For low river flow, SSC increased at Tancarville and decreased at Balise A (e.g., June–July 2015) as the ETM translated upstream. Conversely for high river flow, SSC decreased at Tancarville and increased at Balise A (e.g., January–February 2015) as the ETM translated downstream. Measurements presented a high sensitivity of SSC dynamics to Seine river flow changes, as observed in May 2015.

The measured SSC is reasonably well simulated (red, average over the 5 × 5 cells) at the different locations both in terms of magnitude and neap/spring phasing, with nonetheless a notable underestimation at Fatouville, especially during lower river flow. The hydrological phasing was also consistent with observations, with increasing SSC at Balise A when the river flow increased (i.e., downstream-translated ETM) and increasing SSC at Tancarville when the river flow decreased (i.e., upstream-translated ETM). The SSC at Fatouville and Tancarville during low river flow is frequently underestimated (e.g., July 2015), implying that the ETM is likely to be simulated too far downstream during this period. However, note that Fatouville and Tancarville measurements at pier base close to rocky shore likely yield too high concentration values. Considering the long-term (a year) in situ measurement, SSC simulations have satisfactory skills (Figures 5c, 5e, and 5g; log-log scale) both for the tide-averaged 50th percentile ($r^2_{p50} = 0.57$–0.60) and 90th percentile ($r^2_{p90} = 0.45$–0.62). Model confidence level and error margin associated with the simulated SSC are discussed further in section 3.5.

3.4.2. High-Frequency Suspended Sediment Dynamics

Similar to Figure 5, near-bottom SSC dynamics are presented in Figure 6, but for high-frequency (15 min) concentration, during high (left; 21–23 January 2015) and mean (right; 19–21 April 2015) river flow. The bed shear stress (Figures 6b and 6h) was mainly induced by currents rather than by waves (not shown). Shaded areas represent measurement uncertainty ($c_{cal} = 0.00121 \pm 50\%$, section 2.3) of SSC (light-blue) and

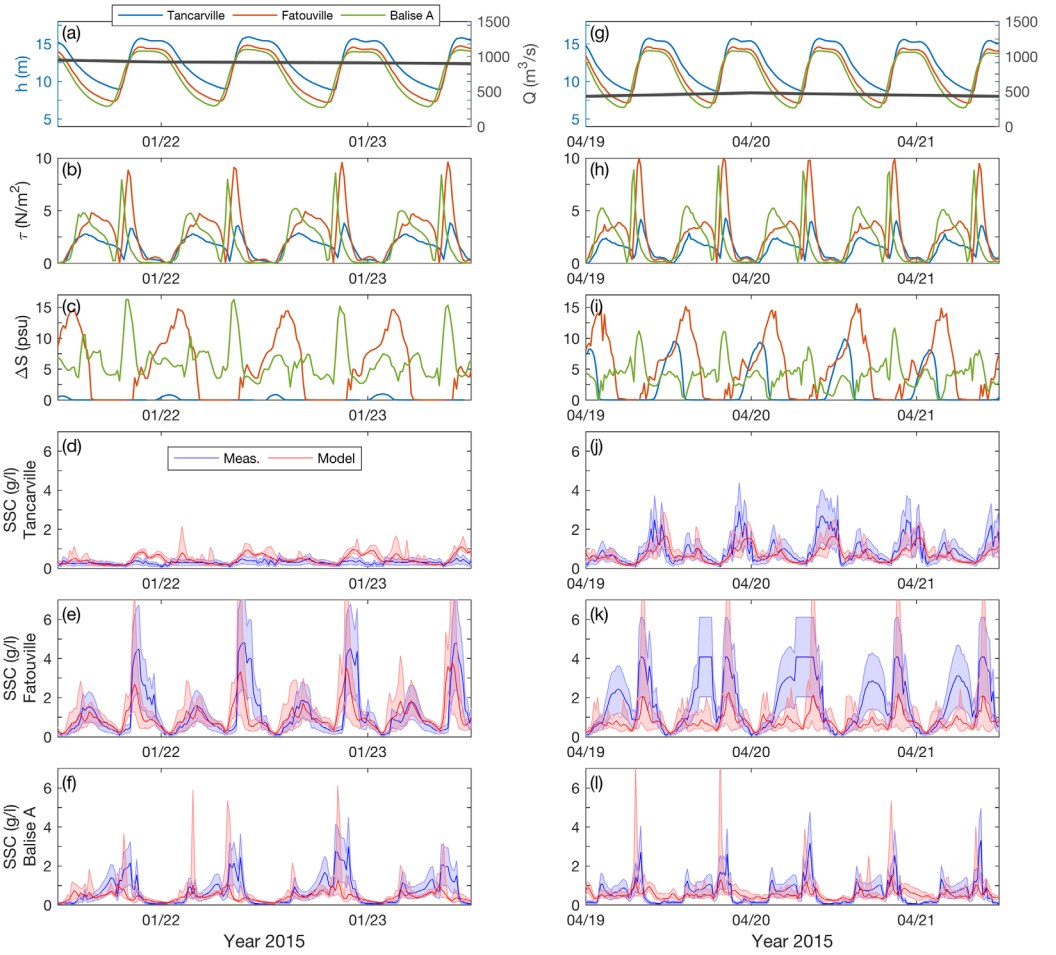

Figure 6. High-frequency (15 min.) near-bottom SSC dynamics for (left) high river flow (21–23 January 2015) and (right) mean river flow (19–21 April 2015). (a, g) Seine river flow Q (gray), water depth h, (b, h) bed shear stress τ, and (c, i) vertical salinity gradient ΔS simulated at Balise A (green), Fatouville (red), and Tancarville (blue). (d–f, j–l) Measured (blue) and simulated (red) SSC at (c, h) Tancarville, (d, i) Fatouville, and (e, j) Balise A. For simulations, light-red areas represent the min/max values in the black boxes defined in Figure 1b; for measurements, light-blue areas represent the 50% error margin associated with the SSC calibration coefficient. Turbidimeter saturation can be noticed at Fatouville in April 2015 (i).

simulation variability (i.e., minimum and maximum values) over the 5 × 5 cells (light-red). The SSC measured at the different stations clearly shows the influence of river flow on turbidity measurements. The ETM was located downstream of Tancarville during high river flow (low concentration at Tancarville in January 2015) while it extended from Balise A to Tancarville during mean river flow. SSC peaks were mainly related to bed shear stress peaks during flood and ebb maximum flow velocities, but they were also observed during low tide, especially at Balise A (Figure 6f), characteristic of the ETM advection and settling. The SSC peaks were weaker during ebb phases than during flood phases. It is related to the reduced bed shear stress and to the enhance stratification (Figures 6c and 6i) that take place during ebb flow.

The model results emphasize the significant spatial variability of SSC within a relatively small area (∼1 to 2 km along, 400–500 m across channel). Such gradients are likely to occur in the field, but have not been investigated in the Seine Estuary yet. McSweeney et al. (2016) explored the importance of lateral variability in sediment transport mechanisms in the ETM-dominated Delaware Estuary. Time series of sediment transport revealed a consistent pattern of sediment export across the entire estuary during periods of high river flow, followed by a transition to import within the channel and export on the flanks during low river flow. Schulz et al. (2018) discuss the residual sediment fluxes in the main channel and on the intertidal flanks at seasonal and yearly time scales. However, the intra-channel lateral variability of the Seine Estuary, which is strongly confined by dykes, is not discussed.

As observed in Figure 5, the SSC is underestimated at Fatouville during mean river flow, especially during ebb (Figure 6k). The simulated sediment suspension is more responsive to the first half of the ebb than to the second half, contrarily to the measurements. In addition, the SSC peaks measured at Balise A during low tide are generally underestimated by the model (Figures 6f and 6l). Such near-bottom SSC peaks are likely to be associated with the ETM settling as they occur at slack water when the bed shear stress is close to zero. On the whole, the ebb/flood tidal phasing and SSC magnitude are reasonably well simulated at the three locations and the SSC response to river flow changes, clearly readable at Tancarville, is in agreement with measurements (Figures 6c–6j).

As presented in section 2.2.2, the GPMH and the GPMR carry out significant dredging and dumping activities, principally for channel maintenance, representing large anthropogenic transfers of sediment mass (∼5.4 Mt/yr) along the lower estuary. Encouragingly, the schematic modeling of sediment dredging and dumping adopted in this study (see section 2.2.2) provides fairly good agreement with observations. For instance, in 2010–2011, the model dredged 3.4 Mt/yr for GPMR areas (3.8 Mt/yr measured) and 2.0 Mt/yr for GPMH areas (1.6 Mt/yr measured). Simulated dredged sediment for GPMH was mainly mud (65%), consistent with observations (85%); however, it was muddy sand (13% mud and 64% fine sand) for GPMR, whereas observed dredged sediment was sandy mud (66% mud and 28% fine sand).

3.5. Quantification of Error Margin for Simulated SSC

Realistic numerical modeling of mud/sand dynamics in macrotidal estuaries is associated with errors that have to be quantified to evaluate the confidence level in simulated results. Hydrodynamics and hydrology modeling provides good skills and most of the simulation errors arise from modeling the complex suspended sediment dynamics. The SSC error margin is discussed at high-frequency (15 min) and tidal time scales (Figures 7d–7f), associated with the respective occurrence probability (Figures 7a–7c). Most of the time (81–95%), the error margin at Balise A, Fatouville, and Tancarville ranges between 23 and 34% (normalized $e_{rms} = 0.23–0.34$). During high-concentration events (1–7% of the time), the error margin ranges between 60 and 80% (Figures 7a and 7d). At tide-averaged time scales, the error margin for median SSC (50th percentile) is always smaller than 50% (Figures 7b and 7e); the error margin for the 90th percentile SSC reaches a maximum of 63–65% during high-concentrated events (11% of the time) at Fatouville (Figures 7c and 7f).

The error margins are mainly related to SSC underestimation, especially at Fatouville and Tancarville. Nonetheless, they have to be put in perspective to the fact that the in situ measurements at Fatouville and Tancarville monitoring stations are likely to overestimate the SSC due to local phenomena (see section 2.3). Consequently, the confidence level that can be attributed to the quantification of the Seine Estuary SSC

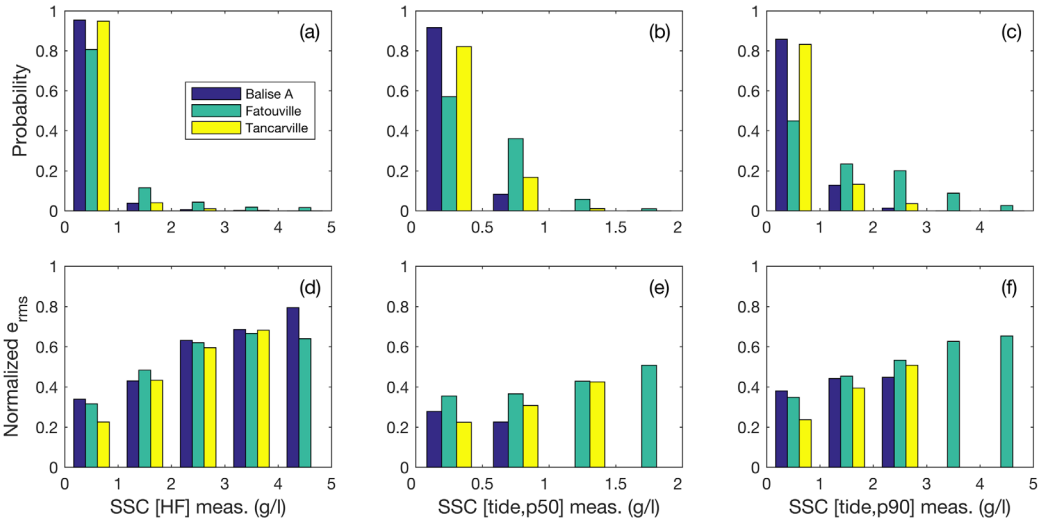

Figure 7. (top) Occurrence probability distribution and (bottom) normalized root-mean-square error of measured: (a, d) high-frequency (15 min) SSC, (b, e) 50th percentile of tide-averaged SSC, and (c, f) 90th percentile of tide-averaged SSC. Comparisons at Balise A (blue), Fatouville (green), and Tancarville (yellow).

dynamics is expected to be associated with an error margin lower than 50% at tide-averaged time scales. Such results, based on 1 year high-frequency measurements carried out at three locations and simulations ran after a one-year spin-up, provide a satisfactory level of confidence to investigate the suspended sediment dynamics of a macrotidal estuary from tidal to yearly time scales (e.g., Amoudry et al., 2014; Bi & Toorman, 2015; Toublanc et al., 2016; Yu et al., 2014).

4. Analysis of ETM Location and Mass Dynamics

Based on the numerical modeling of SSC dynamics from August 2014 to August 2015 presented in section 3.4, this section aims at investigating and quantifying the ETM dynamics focusing on the ETM location and mass changes. These ETM characteristics are based on the suspended mud class and are discussed with regard to the main estuarine forcing, i.e., the river flow, tides, and waves.

4.1. Method to Estimate ETM Location and Mass

The Seine suspended sediment is confined by dykes along the main channel from upstream of Tancarville down to Balise A (blue lines in Figure 1b). Sediment resuspensions are observed at the estuary mouth on the shallow banks, but they have specific dynamics and do not merge with the maximum turbidity zone observed between Balise A and Tancarville from low to high river flow. Figures 8a–8f illustrates instantaneous mud SSC in the lower estuary at flood mid-tide "MT,flood" (i.e., mean sea level at Fatouville during the flood phase) with tidal range $TR = 6.1$ m for low ($Q = 400$ m^3/s) and high ($Q = 1{,}000$ m^3/s) river flow. The ETM area is defined as the estuarine channel between the dykes from the kilometric point kp 370 at the mouth to kp 320 upstream (Figures 8c and 8d). The high-concentrated SSC zone is translated downstream during high river flow, but remains in the ETM area for $Q = [200–1{,}200]$ m^3/s observed in 2014–2015 (Figures 8d and 8f).

The ETM location estimate is based on the high-frequency (15 min) depth- and across-channel-averaged mud SSC transects from pk 320 to pk 370 (Figures 8c, 8d, 8g, and 8h). As the maximum of the SSC transect can be difficult to detect due to spiky local resuspensions, the ETM location is estimated as the median of the SSC transect, as illustrated in Figures 8g and 8h (triangles) for four characteristic tidal phases (low tide "LT," flood mid-tide "MT, flood," high tide "HT," and ebb mid-tide "MT, ebb"; with "MT, ebb" corresponding to mean sea level at Fatouville during the ebb phase). These high-frequency ETM locations represent the ETM excursion during semidiurnal tidal cycles. In section 4.2, in order to remove the semidiurnal ETM variability, the tide-averaged ETM location x_{ETM} is defined as the median of the high-frequency ETM locations from low to low tide (vertical dashed line in Figures 8g and 8h).

The high-frequency ETM mass is computed by integrating the high-frequency mud SSC over the above-defined ETM zone. In section 4.3, the tide-maximum ETM mass is defined as the maximum of the high-frequency ETM masses from low to low tide. Note that different methods have been tested. For instance, reducing the ETM area by only considering the SSC 50% larger than the upstream SSC (i.e., $SSC_{ETM} > 1.5 \times SSC_{pk\ 310}$) does not significantly change the ETM location (less than 1 km) and only slightly reduces the ETM mass (less than 5%) during high river flow. Considering the error margin on the 90th percentile SSC (section 3.5), the tide-maximum ETM mass may be underestimated by 50%. However, the underestimation should be smaller during high river flow, when the simulations are in better agreement with the measurements (Figures 5 and 6).

The tide-averaged salinity front location $x_{Salinity}$ is defined as the median (again of the high-frequency output from low to low tide) of the 5 psu location at 1 m above the bed, representing the near-bottom salinity gradient between the fresh river flow and the saline seawater (e.g., red contours in Figures 8e and 8f). Note that using a lower threshold to define the salinity gradient (e.g., 1 instead of 5 psu) changes the absolute location (kp), but does not significantly change its dynamics. In addition, the 5 psu threshold was observed to better represent the longitudinal salinity gradient near the bottom.

4.2. Tide, River Flow, and Wave Influence on ETM Location

Tide and river flow are known to strongly modulate ETM excursion and extension (Allen et al., 1980; Avoine et al., 1981; Sommerfield & Wong, 2011; Van Maren & Hoekstra, 2004). The simulated Seine ETM is in agreement with such dynamics, as illustrated in Figure 9. The tide-averaged ETM location x_{ETM} ranges mostly from Tancarville (kp 338) to Balise A (kp 365) with a yearly average location around Fatouville (kp 350). x_{ETM}

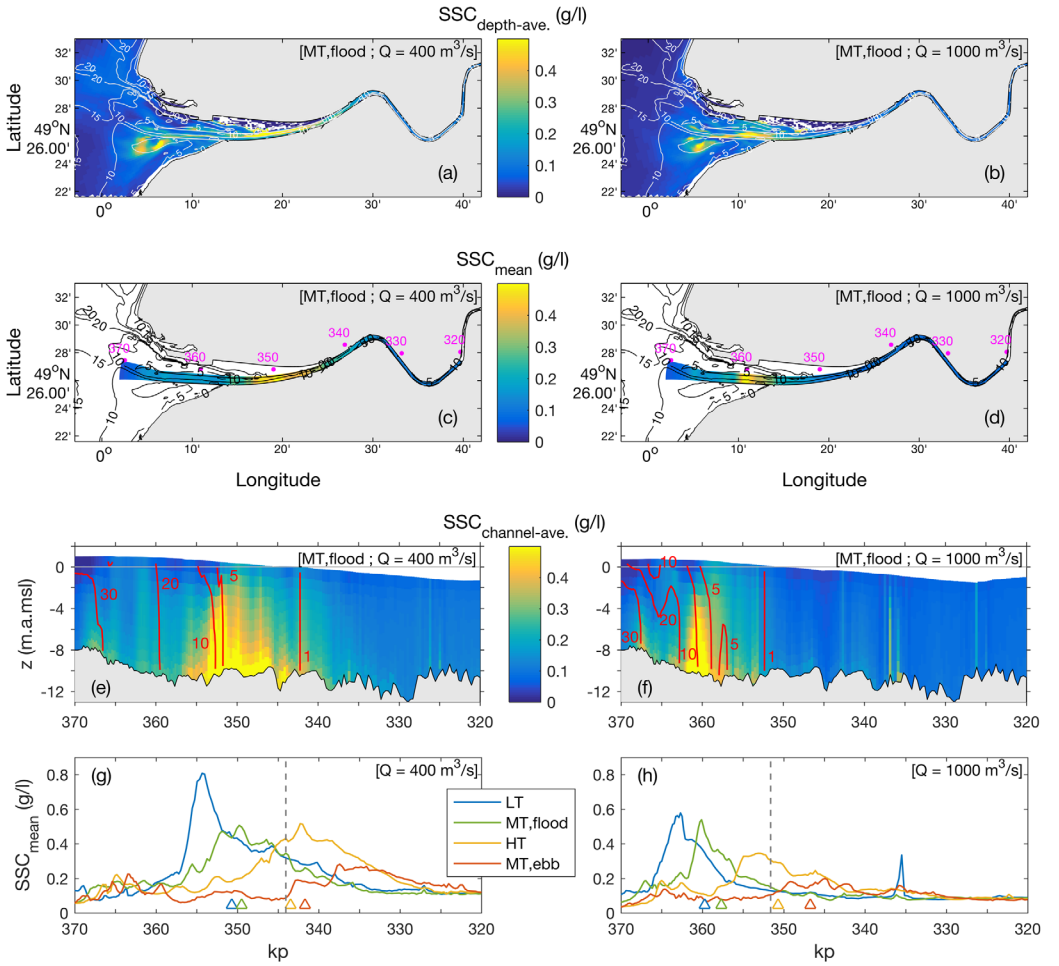

Figure 8. Method and boundaries for estimating de ETM location and mass. Instantaneous SSC simulations (left) on 23 April 2015 during mean river flow $Q = 400$ m^3/s and (right) on 8 May 2015 during high river flow $Q = 1{,}000$ m^3/s. (a, b) Depth-averaged mud SSC at the flood mid-tide (MT,flood) with the bathymetry in white contours, (c, d) depth- and across-channel-averaged mud SSC at the flood mid-tide (MT, flood) in the area defining the ETM computation with the bathymetry in black contours and kilometric points (kp) in magenta, (e, f) vertical profile of across-channel-averaged mud SSC at the flood mid-tide (MT,flood) versus kilometric points (kp) in the area defining the ETM computation, with the across-channel-averaged salinity in red contours, and (g, h) depth- and across-channel-averaged mud SSC versus kilometric points (kp) in the area defining the ETM computation at low tide (LT), flood mid-tide (MT, flood), high tide (HT), and ebb mid-tide (MT,ebb). Triangles represent the ETM locations at times "LT," "MT,flood," "HT," and "MT,ebb"; the vertical dashed-line represents the tide-median ETM location.

is clearly driven by the river flow, translating downstream during high river flow and upstream during low river flow, with a high sensitivity to the river flow changes, as observed in Figure 5 (e.g., May 2015 and February 2015). Accordingly, the salinity front location $x_{Salinity}$ presents a similar high sensitivity to Seine river flow changes. However, it shows a different behavior than the ETM at shorter time scales. x_{ETM} variability associated with semidiurnal tidal cycles (Δx), represented in Figure 9d (gray) and g as the lowermost and uppermost high-frequency ETM locations over a tidal cycle, covers approximately 20 km during spring tides.

4.2.1. River-Flow-Detrended Analysis of ETM and Salinity Front Locations

Fortnightly time scales (i.e., neap/spring tides) seem to affect x_{ETM} and $x_{Salinity}$ dynamics, but the effect is difficult to see in the overlaid signals. Therefore, these signals have to be detrended from the river flow variability to be analyzed with regard to the tidal range TR. x_{ETM} and $x_{Salinity}$ are plotted versus the river flow (Figure 10a), illustrating their strong correlation, and linear regression laws are derived (dashed lines in Figure 10a) to extract the trends associated with Q, as:

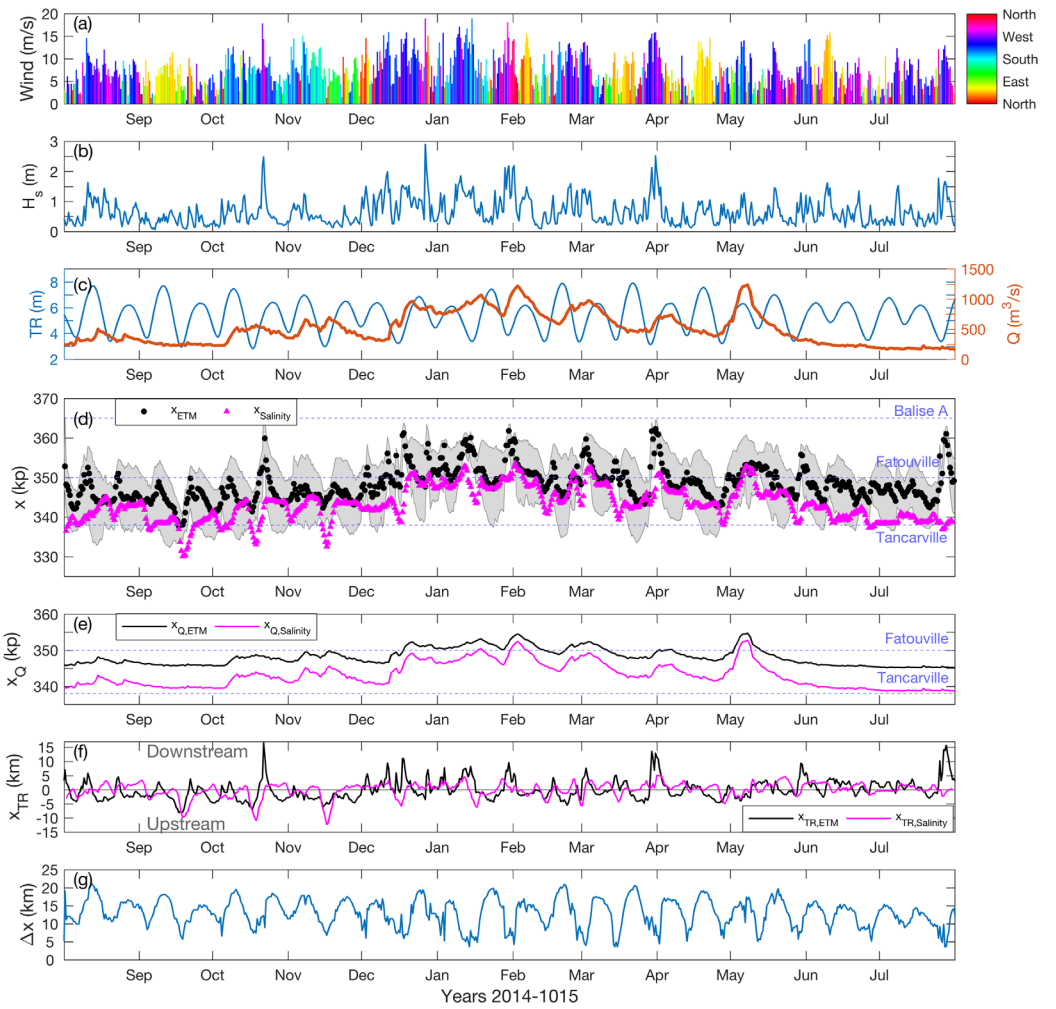

Figure 9. Time evolution of near-bottom salinity front and ETM locations versus hydro-meteorological conditions from August 2014 to August 2015. (a) Wind speed and origin direction (colorbar), (b) significant wave height H_s at the estuary mouth, (c) tidal range TR (blue) and Seine river flow Q measured at Poses (orange), (d) tide-averaged simulated ETM location x_{ETM} (black circles) and salinity front location $x_{Salinity}$ (purple triangles) simulated along the lower estuary. The gray lines represent the lowermost and uppermost ETM locations per semidiurnal tidal cycle. (e) River-flow-induced locations (see equation (9)) of salinity front $x_{Q\ Salinity}$ (purple) and ETM $x_{Q\ ETM}$ (black), (f) river-flow-detrended locations (see equation (9)) of salinity front $x_{TR\ Salinity}$ (purple) and ETM $x_{TR\ ETM}$ (black), and (g) ETM spatial range Δx along a semidiurnal tidal cycle computed as the distance between the lowermost and uppermost ETM locations (gray lines in Figure 9d). In Figures 9d and 9e, the horizontal blue lines represent Tancarville (kp 338), Fatouville (kp 350), and Balise A (kp 365) locations.

$$\begin{cases} x_{Q,ETM,p} = 0.0089 * Q + 343.7 \\ x_{Q,Salinity,p} = 0.0131 * Q + 336.4 \end{cases} \tag{8}$$

Then, the location variabilities associated with the tidal range read:

$$\begin{cases} x_{TR,ETM} = x_{ETM} - x_{Q,ETM,p} \\ x_{TR,Salinity} = x_{Salinity} - x_{Q,Salinity,p} \end{cases}. \tag{9}$$

The decomposition of the ETM and salinity front locations through the river-flow-induced components (x_Q) and river-flow-detrended components (x_{TR}) are represented in Figures 9e and 9f, respectively. $x_{TR,ETM}$ and $x_{TR,Salinity}$ showed different variations that may be related to fortnightly time scales. It appears that very energetic wave events could affect the ETM location due to large wave-induced resuspension at the mouth; nonetheless, waves had little influence most of the time.

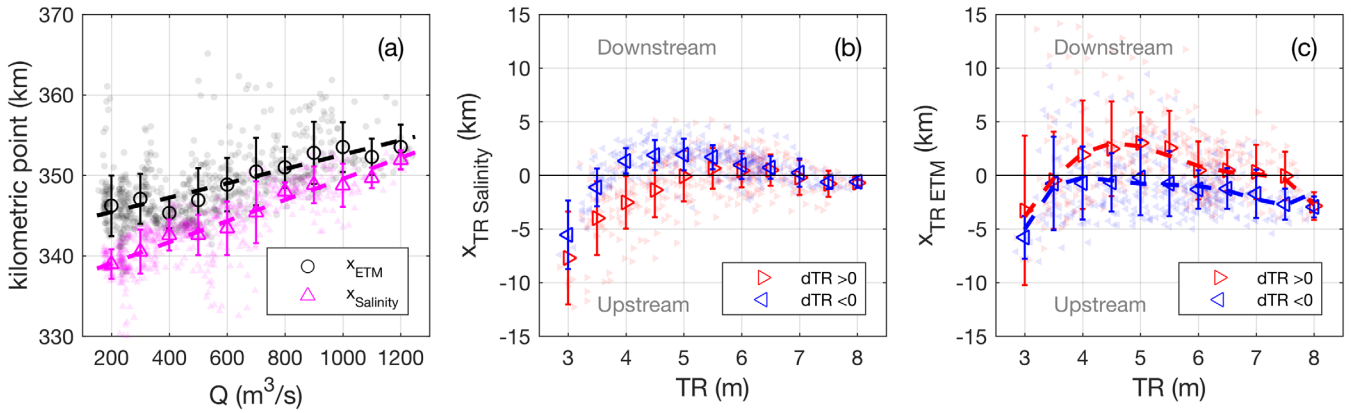

Figure 10. (a) Simulated ETM and salinity front locations, x_{ETM} and $x_{Salinity}$, versus the Seine river flow Q. River-flow-detrended locations (see equation (9)) of (b) near-bottom salinity front $x_{TR\ Salinity}$ and (c) ETM $x_{TR\ ETM}$ versus tidal range TR for neap-to-spring ($dTR > 0$, light-red circles) and spring-to-neap ($dTR < 0$, light-blue circles) phasing. In Figure 10a, black and purple lines represent linear regression laws for x_{ETM} and $x_{Salinity}$, respectively; symbols and vertical bars represent data average and standard deviation, respectively, associated with Q ranges (100 m^3/s). In Figures 10b and 10c, triangles and vertical bars represent data average and standard deviation, respectively, associated with TR ranges (0.5 m) for neap-to-spring (red rightward triangles) and spring-to-neap (blue leftward triangles) phasing.

To investigate the influence of neap/spring phasing on ETM and salinity front locations, $x_{TR,ETM}$ and $x_{TR,Salinity}$ are analyzed versus the tidal range TR. It appears clearly in Figure 10b that the salinity front is located further upstream ($x_{TR\ Salinity} < 0$) for low tidal ranges (TR = [3–4] m). This characteristic is related to stratification during lowly energetic periods (neap tide). However, there is a hysteresis response to the neap-to-spring phasing, showing an anticlockwise pattern. This phasing is illustrated with the tidal range changes (dTR), computed at a given tide t as:

$$dTR_t = \frac{TR_{t+1} - TR_{t-1}}{2} \tag{10}$$

where $dTR > 0$ defines a neap-to-spring period (increasing tidal range) and $dTR < 0$ defines a spring-to-neap period (decreasing tidal range). For a given TR between 3 and 5 m, the salinity front is located further downstream for spring-to-neap tides ($dTR < 0$, blue) than for neap-to-spring tides ($dTR > 0$, red). This difference can be explained by the delay for stratification to fully develop. In other words, during spring tide the water column is mainly mixed and homogenous, but with decreasing TR (i.e., spring-to-neap phasing, blue) the stratification slowly develops until it reaches its maximum at neap tide, associated with an upward migration of the near-bottom salinity front (Burchard & Hetland, 2010). Nonetheless, stratification seems to start to develop only in the second half of the spring-to-neap phase, when $TR < 5$ m.

The ETM dynamics in Figure 10c present a distinct trend. While the ETM is located further upstream ($x_{TR\ ETM} < 0$) during low tidal range (TR = 3 m), probably resulting from the salinity front dynamics, it is also located further upstream during high tidal range (TR = [7–8] m), which is characteristic of the tidal pumping mechanism (Toublanc et al., 2016; Yu et al., 2014). There is also a hysteresis response to the neap-to-spring tidal phasing, but showing a clockwise pattern. This means that for a given TR between 4 and 7.5 m, the ETM is located further downstream for neap-to-spring tides ($dTR > 0$, red) than for spring-to-neap tides ($dTR < 0$, blue). Such a hysteresis can be explained by the delay of the ETM to reach its equilibrium location, forced by the tidal pumping.

These results indicate that the Seine ETM location is driven by the salinity gradients for neap tide (TR = [3–5] m) and by the tidal pumping for spring tide (TR = [5–8] m). It would be interesting to further investigate the hysteresis mechanism with regard to different ETM-dominated estuaries; however, it is beyond the scope of this study.

4.2.2. Quantification of Estuarine Forcing Influence on ETM Location

The influence of estuarine forcing on ETM location changes can be quantified, the location range is: ~10 km for river flow between 150 and 1,250 m^3/s (Figure 10a), ~20 km for the semidiurnal tidal cycle (Figure 9g) and ~8.5 km for the fortnightly time scales (Figure 10c). Note that the neap-to-spring phasing is not negligible as it can modulate the ETM location by ~3 km during moderate tides (TR = [4–6] m; Figure 10c). In addition, an empirical formulation can be derived from these results to estimate $x_{TR,ETM}$ from TR, as:

Table 2
Empirical Coefficients Associated With the Equations (11) and (13)

Coefficient	$n=5$	$n=4$	$n=3$	$n=2$	$n=1$	$n=0$
$a_{n\ [dTR>0]}$ (km)	−0.063	1.605	−15.527	69.517	−137.936	88.811
$a_{n\ [dTR<0]}$ (km)	0.094	−2.650	29.356	−160.037	429.167	−453.017
b_n (10^6 kg)	−0.387	11.171	−123.363	659.373	−1,694.510	1,686.916
$b_{n\ [dTR>0]}$ (10^6 kg)	0.128	−2.761	23.877	−99.379	202.768	−153.550
$b_{n\ [dTR<0]}$ (10^6 kg)	−0.896	24.838	−267.233	1,399.024	−3,542.489	3,480.245

$$x_{TR,\ ETM,p}=a_5.TR^5+a_4.TR^4+a_3.TR^3+a_2.TR^2+a_1.TR+a_0, \tag{11}$$

with distinctive empirical coefficients a_n for $dTR>0$ and $dTR<0$ (dashed lines in Figure 10c; Table 2). Then, the predicted ETM location reads:

$$x_{ETM,p}=x_{Q,ETM,p}+x_{TR,ETM,p}. \tag{12}$$

The prediction skills remain moderate ($r^2=0.42$ and $e_{rms}=3.1$ km; Figures 13a and 13b); however, the simple empirical formula may be useful for the Seine estuary managers.

4.2.3. Diachronic Comparison of ETM Location From 1980 to 2015

A comparison between the ETM location estimated by Avoine et al. (1981) in 1978 and simulated by the present model from August 2014 to August 2015 is illustrated in Figure 11 for different Seine river flows and high-tide and low-tide periods. Avoine et al. (1981) estimated the uppermost (high tide) and lowermost (low tide) ETM locations based on the maximum SSC measured during few tidal cycles (solid black triangles). The river flow influence is clearly readable in both cases. The simulations show that the ETM uppermost limit did not change notably during the last 35 years; however, the seaward limit migrated few kilometers (up to 10 km) further upstream in 2014–2015, especially for average river flow (i.e., 400–600 m^3/s).

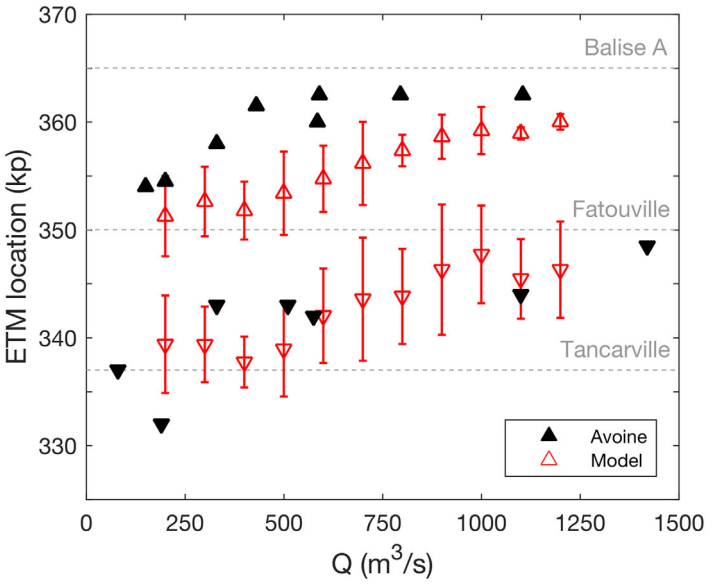

Figure 11. ETM location versus the Seine river flow Q at high tide (downward triangles) and low tide (upward triangles) estimated by Avoine et al. (1981) in 1978 from turbidity measurements (solid black) and based on the median of SSC simulated with the present model (open red) from August 2014 to August 2015. Vertical bars represent the simulated ETM location variability (standard deviation) due to semidiurnal and fortnightly tidal cycles associated with river flow ranges (100 m^3/s). Horizontal gray lines represent Tancarville (kp 338), Fatouville (kp 350), and Balise A (kp 365) locations.

The recent in situ measurements corroborate this tendency and even suggest that the ETM should be slightly upstream of the simulated location. For instance, at Fatouville during ebb flow (Figure 6d), the phasing between the measured and simulated SSC peaks, which represents the ETM advection, is in fair agreement. The simulated SSC peak is slightly early, implying that the simulated ETM location is downstream of the measured one. In addition, the simulations underestimate the SSC at Fatouville and Tancarville during low river flow (e.g., July 2015, Figure 5), suggesting that the ETM may be simulated too far downstream during this period.

Avoine et al. (1981) observed a seaward ETM migration from 1955 to 1978, resulting from the creation of dykes along the main channel to enhance ebb flows. The observed upriver migration of the lowermost ETM location between 1978 and 2015 may result from the extensive GPMH extension in 2001–2006 ("Port 2000"). Such works reduced the northern intertidal mudflat ("Vasière Nord") at the estuary mouth enhancing a funnel-shaped estuary. These changes are likely to increase the tidal asymmetry, enhancing the tidal pumping mechanism and leading to the upstream migration of the ETM. Nonetheless, a diachronic analysis of past (1980s) and current (2010s) simulations would be necessary to thoroughly investigate such ETM dynamic changes, which is out the scope of this paper.

4.3. Tide, River Flow, and Wave Influence on ETM Mass

4.3.1. Tide Influence on ETM Mass

The ETM mass results from the combination of the different formation mechanisms (i.e., tidal pumping, salinity gradient trapping; Brenon & Le Hir, 1999; Dronkers, 1986; Dyer, 1973; Yu et al., 2014). The simulations

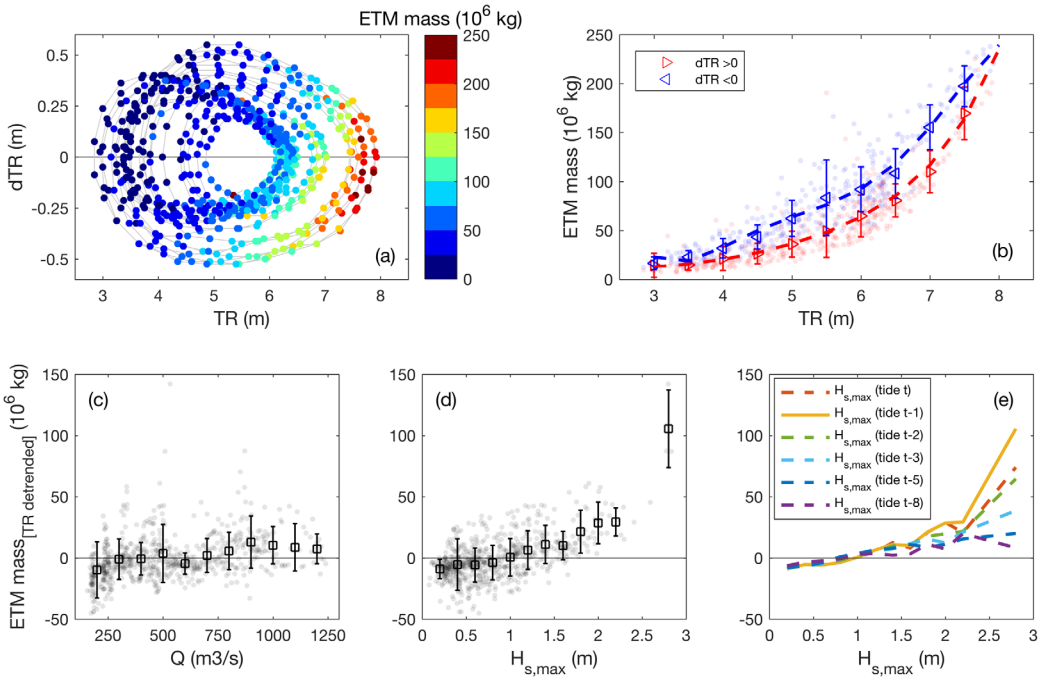

Figure 12. (a, b) Simulated tide-maximum ETM mass versus tidal range *TR* and tidal range changes *dTR*, characterizing neap-to-spring ($dTR > 0$, red circles) and spring-to-neap ($dTR < 0$, blue) phasing. Simulated tide-maximum ETM mass detrended from *TR* variations versus (c) the Seine river flow *Q*, (d) the maximum significant wave height $H_{s,max}$ at tide "*t*-1," and (e) the maximum significant wave height $H_{s,max}$ at tides "*t*," "*t*-1," "*t*-2," "*t*-3," "*t*-5," and "*t*-8." In Figures 12b–12d, symbols and vertical bars represent data average and standard deviation, respectively, associated with abscissa ranges. In Figure 12e, lines represent data average associated with abscissa ranges (*Q*: 100 m^3/s; $H_{s,max}$: 0.2 m) for the reference tide "*t*-1" (continuous) and other tides (dashed). Simulations from August 2014 to August 2015.

highlight an obvious relationship between the tidal range and the ETM mass (Figures 12a and 12b) that reaches 250,000 t during the largest spring tides ($TR = 7.5$–8 m). Note that this estimate may reach 375,000 t according to the 50% error margin discussed in section 3.5. These quantities are in agreement with Avoine et al. (1981) who estimated the ETM mass around 300,000 t during spring tide.

As observed for the salinity front and ETM locations in Figure 10, the neap-to-spring phasing *dTR* appears to significantly influence the ETM mass through a hysteresis response (Figures 12a and 12b). For similar *TR*, the ETM mass is lower for neap-to-spring tides ($dTR > 0$, red) than for spring-to-neap tides ($dTR < 0$, blue), implying that the growth as well as the decay of an ETM take time, i.e., the resuspension and accumulation of sediment starting from neap-tide conditions as well as the settling of sediment starting from spring-tide

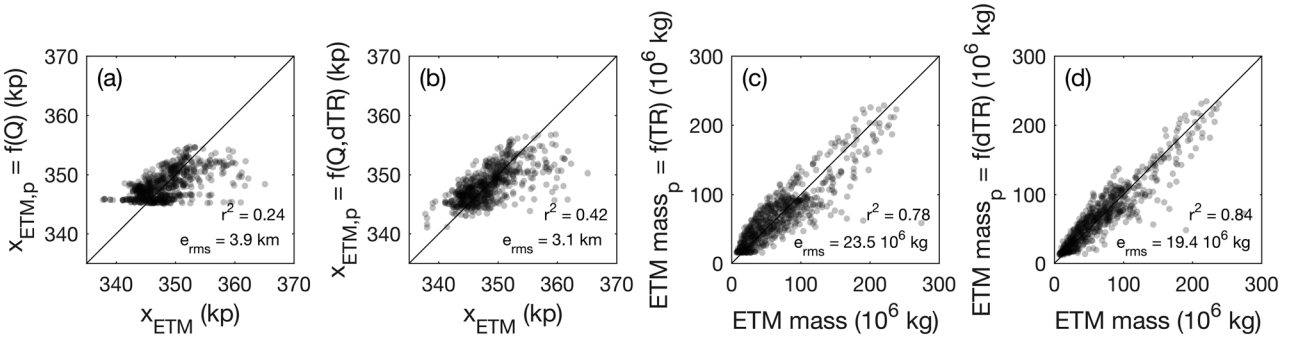

Figure 13. Correlation between simulated ETM location x_{ETM} and predicted ETM location based on (a) river flow *Q* (equation (8)) and (b) river flow *Q*, tidal range *TR*, and tidal phasing *dTR* (equation (12)). Correlation between simulated ETM mass and predicted ETM mass based on (c) tidal range *TR* (equation (13) with b_n) and (d) tidal range *TR* and tidal phasing *dTR* (equation (13) with $b_{n\ [dTR]}$).

conditions. This is in agreement with the delay observed in Figure 10c for the tidal pumping to translate the ETM upstream.

The anticlockwise pattern observed in Figure 12b can provide a relatively accurate relation to estimate the ETM mass based on *TR* and modulated by *dTR*, such as:

$$ETM\ mass_p = b_5.TR^5 + b_4.TR^4 + b_3.TR^3 + b_2.TR^2 + b_1.TR + b_0, \quad (13)$$

with distinctive empirical coefficients b_n for $dTR > 0$ and $dTR < 0$ (dashed lines in Figure 10c; Table 2). The prediction skills are very good ($r^2 = 0.84$ and $e_{rms} = 19.4 \times 10^6$ kg; Figures 13c and 13d), providing an interesting and simple formula to predict the ETM mass.

4.3.2. TR-Detrended Analysis of River Flow and Wave Influence on ETM Mass

The tidal range clearly drives the ETM mass; however, the influence of the river flow and waves have to be quantified. Following a similar method as for the ETM location, the ETM mass signal is detrended from the tidal range variability to be analyzed with regard to the river flow and waves. The empirical formulation $ETMmass_p$ derived from the Figure 13b (dashed lines; equation (13) with $b_{n\ [dTR]}$; Table 2) is used to extract the trends associated with *TR* and *dTR*. Then, the *TR*-detrended ETM mass reads:

$$ETM\ mass_{TR\ detrended} = ETM\ mass - ETM\ mass_p. \quad (14)$$

Interestingly, the river flow in the range 200–1,200 m^3/s does not significantly affect the ETM mass ($+20 \times 10^6$ kg; Figure 12c). During a flood period (e.g., $Q = 1{,}500\ m^3/s$), the river sediment supply cumulated over a semidiurnal tidal cycle (~12 h 25 min) reaches a maximum of 13×10^6 kg (cf. section 2.2.2 and Schulz et al., 2018), whereas the ETM mass can reach 250×10^6 kg. Consequently, the river sediment supply can contribute approximately 5% of the total ETM mass. This is agreement with Amoudry et al. (2014) who observed in the hypertidal Dee Estuary that the sediment input from the river is found to have very little importance on SSC.

Nonetheless, with an annual supply of 725×10^6 kg, the Seine sediment supply is likely to substantially contribute in maintaining enough mud in the estuarine system over the year, especially for very large river flow (i.e., *Q* around 2,000 m^3/s) when the ETM may be flushed out of the estuary mouth. These results imply that the river flow influences only the ETM location (Allen et al., 1980; Avoine et al., 1981; Sommerfield & Wong, 2011; Uncles & Stephens, 1989; Van Maren & Hoekstra, 2004).

Conversely, wave actions have little effect on the ETM location (Figure 9), but can significantly influence the ETM mass (e.g., Le Hir et al., 2001). The simulated waves in front of the estuary mouth were spatially averaged to define the wave forcing used in this study, as for Schulz et al. (2018). The main concern is to determine the time lag between the wave events and the increased ETM mass. In other words, what is the time lag required for wave-induced sediment resuspension to contribute to the ETM mass? The method consists of computing the ETM mass at a tide *t*, and computing the maximum significant wave height per tide $H_{s,max}$ for the 10 previous tides ($t_n = [t\text{-}10{:}t]$). Hence, the time lag is defined as the tide t_n for which the largest correlation between the ETM mass(*t*) and $H_{s,max}(t_n)$ is observed.

As illustrated in Figure 12e, the largest correlation between the ETM mass and $H_{s,max}$ is observed for the tide "*t*-1" and decreases rapidly for time lags longer than tide "*t*-2." The correlation being lower for $H_{s,max}$ computed at tide "*t*" than "*t*-1" highlights that the wave-induced resuspension does not significantly occur in the ETM area, but requires a time lag to be advected toward it. This is in agreement with the simulated bed shear stress being dominated by tidal currents in the ETM zone (Figures 6b and 6h).

The *TR*-detrended ETM mass increases significantly with $H_{s,max}$ (computed at "*t*-1"), with $+40 \times 10^6$ kg for $H_{s,max} = 2$ m, up to $+110 \times 10^6$ kg for $H_{s,max} = 2.8$ m (with respect to $H_{s,max} = 0$ m; Figure 12d). As the maximum ETM mass varies with the tidal range (Figure 13b), the relative wave-induced contribution to the ETM mass varies with *TR* as well. Therefore, wave events can contribute up to 44% of the ETM mass during spring tides ($TR = 8$ m) and up to 230% during mean tides (TR = 5.5 m). This means that wave actions can increase the ETM mass by a factor of 3 during mean tides.

Such energetic wave events explain the scattering observed in Figure 12b. For instance, during a mean tide ($TR = 5.5$ m) associated with very energetic wave conditions ($H_{s,max} = 2.8$ m), the ETM mass (190×10^6 kg) is more than 3 times larger than the mass average (48×10^6 kg) (see high point in Figure 13b for $TR = 5.5$ m corresponding to the high point in Figure 13d for $H_{s,max} = 2.8$ m). As a consequence, not considering wave forcing may result in significantly underestimating the ETM mass during energetic wave conditions.

5. Conclusions

The hydrodynamics and suspended sediment dynamics of the macrotidal Seine Estuary were investigated from semidiurnal tidal cycles to fortnightly time scales and a hydrological year. High-frequency in situ measurements located in the lower estuary provide an extensive insight into the ETM dynamics. A realistic 3D process-based mixed-sediment (i.e., mud, sand, and gravel) numerical model, forced by wind, waves, tides, and river flow, reasonably well simulated the observed dynamics. Nevertheless during low river flow, the numerical model tends to underestimate the sediment concentration in the ETM area.

The simulations provide evidences that the seaward ETM location nowadays (i.e., years 2014–2015) is situated up to 10 km upstream of the location in 1978. It appears that the Seine ETM location is dominated by the tidal pumping mechanism for spring tide and dominated by the salinity gradients for neap tide. Moreover, the tidal range change, characterizing the neap-to-spring (and spring-to-neap) period, significantly influences the ETM location through a hysteresis response due to the delay for tidal pumping and stratification to fully develop.

The ETM mass is highly related to the tidal range, reaching 250,000 t for spring tide, and modulated by the tidal range changes. In addition, the relationship between ETM mass and tidal range proves to be nonlinear, with a clear resuspension increase for tidal range larger than 6 m. However, it clearly appears that the river flow does not significantly affect the ETM mass if the ETM is not flushed out of the estuary, whereas it strongly controls the ETM tide-averaged location. Conversely, wave events substantially influence the ETM dynamics by contributing up to 44% of the ETM mass during spring tides. Furthermore, very energetic wave conditions can increase the ETM mass by a factor of 3 during mean tides.

Based on the model results, empirical formulations have been derived to predict the ETM location and mass from the tidal range and the river flow. Prediction skills are moderate for estimating the ETM locations and very good for estimating the ETM mass, providing simple tools for the Seine Estuary managers.

Finally, the hysteresis response of ETM location and mass to neap-to-spring phasing that is observed in the Seine Estuary would be interesting to compare to other ETM-dominated estuaries, as it provides insight into the delay for tidal pumping and stratification to develop.

Acknowledgments
This study has been carried out in the framework of the HYMOSED project funded by the Seine-Aval 5 research program. It benefited from developments and in situ measurements carried out in the projects MODEL, COLMATAGE, and SUSPENSE and from the SYNAPSES monitoring network (GIPSA, Seine-Aval 4 et 5 research programs). Data are available on http://www.seine-aval.fr/synapses/. Bathymetric data and tidal gauge elevation have been provided by the Grand Port Maritime de Rouen. The authors acknowledge Matthias Jacquet, Hervé Jestin, and David Le Berre for their support on carrying out field measurements and Fabrice Ardhuin and Mickael Accensi for their support with WW3 simulations. We thank the two anonymous reviewers, the Associate Editor, and the Editor for their constructive comments helping us to improve this manuscript.

References

Allen, G. P., Salomon, J., Bassoullet, P., Du Penhoat, Y., & De Grandpre, C. (1980). Effects of tides on mixing and suspended sediment transport in macrotidal estuaries. *Sedimentary Geology*, *26*(1), 69–90.

Amoudry, L. O., Ramirez-Mendoza, R., Souza, A. J., & Brown J. M. (2014). Modelling-based assessment of suspended sediment dynamics in a hypertidal estuarine channel. *Ocean Dynamics*, *64*(5), 707–722.

Avoine, J., Allen, G., Nichols, M., Salomon, J., & Larsonneur, C. (1981). Suspended-sediment transport in the Seine estuary, France: Effect of man-made modifications on estuary—Shelf sedimentology. *Marine Geology*, *40*(1–2), 119–137.

Bi, Q., & Toorman, E. A. (2015). Mixed-sediment transport modelling in Scheldt estuary with a physics-based bottom friction law. *Ocean Dynamics*, *65*(4), 555–587. https://doi.org/10.1007/s10236-015-0816-z

Billen, G., Garnier, J., Nemery, J., Sebilo, M., Sferratore, A., Barles, S., . . . Benoît, M. (2007). A long-term view of nutrient transfers through the Seine river continuum. *Science of the Total Environment*, *375*(1), 80–97.

Brenon, I., & Le Hir, P. (1999). Modelling the turbidity maximum in the Seine estuary (France): identification of formation processes. *Estuarine, Coastal and Shelf Science*, *49*(4), 525–544.

Burchard, H., & Baumert, H. (1998). The formation of estuarine turbidity maxima due to density effects in the salt wedge. A hydrodynamic process study. *Journal of Physical Oceanography*, *28*(2), 309–321.

Burchard, H., & Hetland, R. D. (2010). Quantifying the contributions of tidal straining and gravitational circulation to residual circulation in periodically stratified tidal estuaries. *Journal of Physical Oceanography*, *40*(6), 1243–1262.

Cugier, P., & Le Hir, P. (2002). Development of a 3D hydrodynamic model for coastal ecosystem modelling. Application to the plume of the Seine River (France). *Estuarine, Coastal and Shelf Science*, *55*(5), 673–695.

Deloffre, J., Lafite, R., Lesueur, P., Lesourd, S., Verney, R., & Guézennec, L. (2005). Sedimentary processes on an intertidal mudflat in the upper macrotidal Seine estuary, France. *Estuarine, Coastal and Shelf Science*, *64*(4), 710–720. https://doi.org/10.1016/j.ecss.2005.04.004

Deloffre, J., Verney, R., Lafite, R., Lesueur, P., Lesourd, S., & Cundy, A. B. (2007). Sedimentation on intertidal mudflats in the lower part of macrotidal estuaries: Sedimentation rhythms and their preservation. *Marine Geology*, *241*(1–4), 19–32. https://doi.org/10.1016/j.margeo.2007.02.011

Dronkers, J. (1986). Tide-induced residual transport of fine sediment. In *Physics of shallow estuaries and bays* (pp. 228–244). New York, NY: Springer-Verlag.

Dyer, K. R. (1973). *Estuaries: A physical introduction*. New York, NY: John Wiley.

Geyer, W. R. (1993). The importance of suppression of turbulence by stratification on the estuarine turbidity maximum. *Estuaries*, *16*(1), 113–125.

Grasso, F., Le Hir, P., & Bassoullet, P. (2015). Numerical modelling of mixed-sediment consolidation. *Ocean Dynamics*, *65*(4), 607–616.

Jalón-Rojas, I., Schmidt, S., & Sottolichio, A. (2015). Turbidity in the fluvial Gironde Estuary (Southwest France) based on 10 year continuous monitoring: sensitivity to hydrological conditions. *Hydrology & Earth System Sciences Discussions*, *12*(3).

Jalón-Rojas, I., Schmidt, S., Sottolichio, A., & Bertier, C. (2016). Tracking the turbidity maximum zone in the Loire Estuary (France) based on a long-term, high-resolution and high-frequency monitoring network. *Continental Shelf Research*, *117*, 1–11. https://doi.org/10.1016/j.csr.2016.01.017

Jonsson, I. G. (1966). Wave boundary layers AMD friction factors, *Coastal Engineering Proceedings*, *1*(10), 127–148.

Kervella, Y., Khojasteh Pour Fard, I., Hir, P. L., Renault, E., & Lemoine, J.-P. (2012). *Modélisation hydrodynamique tridimensionnelle en coordonnées curvilignes non-orthogonales de l'estuaire de la Seine*. Paper presented at XIIèmes Journées Nationales Génie Côtier – Génie Civil, Cherbourg, France, 12–14 Juin.

Khojasteh Pour Fard, I. (2015). *Modélisation des échanges dissous entre l'estuaire de la Loire et les baies côtières adjacentes*. Bordeaux, France: University of Bordeaux.

Lazure, P., & Dumas, F. (2008). An external–internal mode coupling for a 3D hydrodynamical model for applications at regional scale (MARS). *Advances in Water Resources*, *31*(2), 233–250.

Le Hir, P., Cann, P., Waeles, B., Jestin, H., & Bassoullet, P. (2008). Erodibility of natural sediments: Experiments on sand/mud mixtures from laboratory and field erosion tests, *Proceedings in Marine Science*, *9*, 137–153.

Le Hir, P., Cayocca, F., & Waeles, B. (2011). Dynamics of sand and mud mixtures: A multiprocess-based modelling strategy. *Continental Shelf Research*, *31*(10), S135–S149. https://doi.org/10.1016/j.csr.2010.12.009

Le Hir, P., Ficht, A., Jacinto, R. S., Lesueur, P., Dupont, J.-P., Lafite, R., . . . Cugier, P. (2001). Fine sediment transport and accumulations at the mouth of the Seine estuary (France). *Estuaries*, *24*(6), 950–963.

Lesourd, S., Lesueur, P., Fisson, C., & Dauvin, J.-C. (2015). Sediment evolution in the mouth of the Seine estuary (France): A long-term monitoring during the last 150years, *Comptes Rendus Geoscience*, *348*, 442–450.

Marmin, S., Dauvin, J. C., & Lesueur, P. (2014). Collaborative approach for the management of harbour-dredged sediment in the Bay of Seine (France). *Ocean & Coastal Management*, *102*, 328–339. https://doi.org/10.1016/j.ocecoaman.2014.10.012

McSweeney, J. M., Chant, R. J., & Sommerfield, C. K. (2016). Lateral variability of sediment transport in the Delaware Estuary. *Journal of Geophysical Research: Oceans*, *121*, 725–744. https://doi.org/10.1002/2015JC010974

Panagiotopoulos, I., Voulgaris, G., & Collins, M. (1997). The influence of clay on the threshold of movement of fine sandy beds. *Coastal Engineering*, *32*(1), 19–43.

Partheniades, E. (1965). Erosion and deposition of cohesive soils. *Journal of the Hydraulics Division*, *91*(1), 105–139.

Passy, P., Le Gendre, R., Garnier, J., Cugier, P., Callens, J., Paris, F., . . . Romero, E. (2016). Eutrophication modelling chain for improved management strategies to prevent algal blooms in the Bay of Seine. *Marine Ecology Progress Series*, *543*, 107–125.

Roland, A., & Ardhuin, F. (2014). On the developments of spectral wave models: Numerics and parameterizations for the coastal ocean. *Ocean Dynamics*, *64*(6), 833–846.

Sanford, L. P. (2008). Modeling a dynamically varying mixed sediment bed with erosion, deposition, bioturbation, consolidation, and armoring. *Computers & Geosciences*, *34*(10), 1263–1283. https://doi.org/10.1016/j.cageo.2008.02.011

Schulz, E., Grasso, F., Le Hir, P., Verney, R., & Thouvenin, B. (2018). Suspended sediment dynamics in the macrotidal Seine Estuary (France): 2. Numerical modelling of sediment fluxes and budgets under typical hydrological and meteorological conditions. *Journal of Geophysical Research: Oceans*, *123*. https://doi.org/10.1002/2016JC012638

Scully, M. E., & Friedrichs, C. T. (2007). Sediment pumping by tidal asymmetry in a partially mixed estuary. *Journal of Geophysical Research*, *112*, C07028. https://doi.org/10.1029/2006JC003784

Simpson, J. H., Brown, J., Matthews, J., & Allen, G. (1990). Tidal straining, density currents, and stirring in the control of estuarine stratification. *Estuaries*, *13*(2), 125–132.

Sommerfield, C. K., & Wong, K. C. (2011). Mechanisms of sediment flux and turbidity maintenance in the Delaware Estuary. *Journal of Geophysical Research*, *116*, C01005. https://doi.org/10.1029/2010JC006462

Sottolichio, A., Castaing, P., Etcheber, H., Maneux, E., Schmeltz, M., & Schmidt, S. (2011). Observations of suspended sediment dynamics in a highly turbid macrotidal estuary, derived from continuous monitoring. *Journal of Coastal Research*, *64*, 1579–1583.

Sottolichio, A., Hir, P. L., & Castaing, P. (2000). Modeling mechanisms for the stability of the turbidity maximum in the Gironde estuary, France, *Proceedings in Marine Science*, *3*, 373–386.

Soulsby, R. (1997). *Dynamics of marine sands: A manual for practical applications*. London: Thomas Telford.

Toublanc, F., Brenon, I., & Coulombier, T. (2016). Formation and structure of the turbidity maximum in the macrotidal Charente estuary (France): Influence of fluvial and tidal forcing. *Estuarine, Coastal and Shelf Science*, *169*, 1–14. https://doi.org/10.1016/j.ecss.2015.11.019

Uncles, R., & Jordan, M. (1979). Residual fluxes of water and salt at two stations in the Severn Estuary. *Estuarine and Coastal Marine Science*, *9*(3), 287–302.

Uncles, R., & Stephens, J. (1989). Distributions of suspended sediment at high water in a macrotidal estuary. *Journal of Geophysical Research*, *94*(C10), 14395–14405.

Van Leussen, W. (1994). *Estuarine macroflocs and their role in fine-grained sediment transport*. The Hague, the Netherlands: Ministry of Transport, Public Works and Water Management, National Institute for Coastal and Marine Management.

Van Maren, D., & Hoekstra, P. (2004). Seasonal variation of hydrodynamics and sediment dynamics in a shallow subtropical estuary: The Ba Lat River, Vietnam. *Estuarine, Coastal and Shelf Science*, *60*(3), 529–540.

Verney, R., Deloffre, J., Brun-Cottan, J. C., & Lafite, R. (2007). The effect of wave-induced turbulence on intertidal mudflats: Impact of boat traffic and wind. *Continental Shelf Research*, *27*(5), 594–612. https://doi.org/10.1016/j.csr.2006.10.005

Waeles, B., Hir, P. L., & Lesueur, P. (2008). A 3D morphodynamic process-based modelling of a mixed sand/mud coastal environment: the Seine estuary, France, *Proceedings in Marine Science*, *9*, 477–498.

Winterwerp, J. C. (2011). Fine sediment transport by tidal asymmetry in the high-concentrated Ems River: Indications for a regime shift in response to channel deepening. *Ocean Dynamics*, *61*(2–3), 203–215.

Yu, Q., Wang, Y. W., Gao, J. H., Gao, S., & Flemming, B. (2014). Turbidity maximum formation in a well-mixed macrotidal estuary: The role of tidal pumping. *Journal of Geophysical Research: Oceans*, *119*, 7705–7724. https://doi.org/10.1002/2014JC010228

Erratum

In the originally published version of this article, there were several incorrect references to Figures 11, 12, and 13 and their subparts in sections 4.2.2. through 4.3.2. This has since been corrected and this version may be considered the authoritative version of record.